COMPUTATIONAL MODELLING STUDY OF LAYERED $LiNiO_2$ SURFACE, SURFACE DOPING AND INTERACTION WITH THE ELECTROLYTE IN LI-ION BATTERIES

A dissertation presented

by

Hiine Mmeshi Jassicon

RESEARCH DISSERTATION

Submitted in fulfillment of the requirements for the degree of

MASTER OF SCIENCE (MSc)

In

Physics

In the

FACULTY OF SCIENCE AND AGRICULTURE

(School of Physical and Mineral Sciences)

at the

University of Limpopo (Turfloop Campus)

SUPERVISOR: Prof K.P. Maenetja

CO-SUPERVISOR: Prof. P.E. Ngoepe

(2025)

DECLARATION

I hereby declare that the dissertation submitted to the University of Limpopo (Turfloop Campus) for the Master of Science degree is my original work in both design and execution. It has not been previously submitted by me for a degree at this or any other university, and all materials included have been properly acknowledged.

26/01/2025

Mr M.J Hiine **Date**

DEDICATION

This work is dedicated to:

My wonderful elder sister

Tshegofatso

My precious late parents

Ngwanarakgomo and Mathiba Hiine

Kea leboga!!

ACKNOWLEDGMENTS

First and foremost, I would like to express my deepest gratitude to God Almighty for His constant guidance, protection, and grace throughout this journey. His strength has sustained me through every challenge, and His wisdom has illuminated my path, making this achievement possible.

I also wish to thank my supervisors and advisors, Professor Khomotso Maenetja, Professor Phuti Ngoepe, and Dr. Brain Ramogayana, for their outstanding mentorship and guidance. Their expertise and encouragement have been instrumental in shaping my research and navigating the complexities of academic work.

The Material Modelling Centre (MMC) members, who kept life interesting by providing numerous occasions to chat about science and life in general.

I am forever grateful to my grandfather, sister, and uncle, whose unwavering support and belief in me have been a constant source of strength, especially through the tough times of losing my parents. Your love has been my greatest motivation.

A special thanks to Dr. Jacob Mothapo, the Material Modelling Centre administrator, for his encouraging words that inspired me to push forward and work harder.

Sponsors of this project: University of Limpopo (UL) and the National Research Foundation (NRF).

Finally, to God be the glory for every success along the way.

Table of Contents

DECLARATION ii

DEDICATION iii

ACKNOWLEDGMENTS iv

ABSTRACT ix

List of Figures xi

List of Tables xii

List of Abbreviations xii

CHAPTER 1 1

Introduction 1

1.1 Background 1

1.1.1 Description of Lithium-ion Batteries 2

1.1.2 Details of a cell's/technical battery's components 4

1.1.3 Applications 5

1.2 Rational 6

1.3 Literature Review 8

1.3.1 Overview 8

1.3.2 Structural aspect of $LiNiO_2$ 9

1.3.3 Cathode Layered Material 11

1.3.4 Spinel $LiMn_2O_4$ 12

1.3.5 Layered $LiCoO_2$ 13

1.3.6 Layered $LiNiO_2$ 15

1.3.7 Layered Surface Doping 16

1.4 Objective 18

1.5 Research Questions 18

1.6 Justification for the Study 19

1.7 Intention of the Study 19

1.8 Outline of the Study 21

CHAPTER 2 22

Theoretical Studies and Computational Methods 22

2.1 Density Functional Theory 22

2.1.1 Approximation Methods 25

2.1.1.1 Local Density Approximation (LDA) 25

2.1.1.2 General Gradient Approximation (GGA) 28

2.2. Plane-wave pseudopotential methods. 31

2.2.1. Plane-Wave Basis Set 31

2.2.2. Pseudopotentials 33

2.2.3. Projector Augmented Wave (PAW) Method 34

2.3. Implications In VASP 35

2.4. Background of the Properties Studied 37

2.4.1. Geometry Optimization 37

2.4.2. Heats of Formation 38

2.4.3 Elastic Properties 39

2.4.4 Phonon Dispersion 41

2.4.5 Density Of state 41

2.4.6 Surface Calculations 42

2.4.7 Surface Stability 43

CHAPTER 3 45

Convergence, mechanical, and vibrational properties of $LiNiO_2$ bulk phase. 45

3.1 METHOD 45

3.2 Convergence test 46

3.3 Structural properties and heats of formation. 48

3.4 Mechanical properties (Elastic Properties) 49

3.5 Electronic properties (band structures and DOS) 52

3.6 Phonon Dispersion 55

3.7 Summary 57

CHAPTER 4 58

4. Surface chemistry of $LiNiO_2$ and effect of organic electrolyte, ethylene carbonate 58

4.1 Method 58

4.2 Surfaces Model and Energies 59

4.3 Surface Free Energies 61

4.4 Density of State 64

4.5 Work function and Bader Charges Analysis 65

4.6 Ethylene Carbonate Adsorption 66

4.7 Summary 70

CHAPTER 5 72

5.1 CONCLUSION 72

5.2 RECOMMENDATION 75

5.3 FUTURE WORK 75

Appendix A: 91

Papers Presented at Conferences 91

Papers to be submitted. 91

ABSTRACT

Lithium-ion batteries have garnered significant attention due to the growing demand for renewable energy sources, with monoclinic $LiNiO_2$ emerging as a promising cathode material. This is attributed to its high specific capacity (275 mAh/g) and energy density (629 Wh/kg). However, its practical application is limited by challenges such as low cycling stability and voltage fading. In this study, the bulk structural properties of $LiNiO_2$ were investigated using first-principles density functional theory, while its low Miller index surfaces were modeled with the METADISE code. The calculated lattice parameters align well with reported data, showing a deviation of less than 2.4%, and the system exhibits a heat of formation of -624.37 kJ/mol, confirming thermodynamic stability. Elastic constant calculations indicate mechanical stability, consistent with monoclinic stability criteria. However, phonon dispersion curves reveal imaginary vibrations in the gamma region, suggesting structural instability. Electronic structure analysis shows that $LiNiO_2$ has an indirect band gap of 0.708 eV near the Fermi level, indicating magnetic metal characteristics. Additionally, various Miller index surfaces ((110), (100), (010), (001), (111), and (101)) were examined, with the (101) facet identified as the most stable surface. The Nb/Mn doping is found to improve the crystal lattice of $LiNiO_2$ and decrease the volume change. We found that after Nb/Mn surface doping, we observed that the surface free energies are lower compared to the surface energy of pure surfaces, indicating that the surface stabilizes upon doping. That the surface free energies of Nb-doped are lower when they are in the second layer compared to when they are in the first layer it implies that the second layer stabilizes the surface more effectively. Whereas the surface free energies of Mn-doped are higher when they are in the second layer compared to when they are in the first layer. The Bader

charge of Nb and Mn are lower in the first layer and the work function in the first layer is higher, which implies that the second layer doped surface is more reactive in the first layer. These findings demonstrate that Nb and Mn doping significantly enhances the surface stability and reactivity of $LiNiO_2$, offering valuable insights for improving its performance as a cathode material in lithium-ion batteries.

List of Figures

Figure 1.1: Charging and discharging phenomenon of Li-ion battery…. 4
Figure 1.2: The various applications of lithium battery 6
Figure 1.3: Crystal structure of layered $LiNiO_2$ and the atomic occupation positions of Li and Ni atoms. 10

Figure 2.1: Schematic diagram for the illustration of an atomic all-electron wavefunction and the corresponding atomic pseudo wavefunction. 34
Figure 2.2: Representation of local and global minima with the transition state 38
Figure 2.3: Representation of how the half-relaxed slab was calculated. The uppermost layers could relax while the lower surfaces were kept fixed at their relaxed bulk positions. 43

Figure 3.1: Graphs of total energy versus the (a) cut-off energy and (b) k-points of $LiNiO_2$. 47
Figure 3.2: Crystal structure of monoclinic $LiNiO_2$. 49
Figure 3.3: Electronic (a) band structure and (b) the DOS showing Li, Ni, and O contribution to the total DOS of $LiNiO_2$. 54
Figure 3.4: The plot of the (a) phonon dispersion curve and (b) partial phonon density of state. 56

Figure 4.1 Shows the directions of different terminations cleaved (a) (101) surface, (b) (001) surface, (c) (100) surface, (d) (011) surface, (e) (110) surface, (f) (010) surface and (g) (111) surface of $LiNiO_2$. 60
Figure 4.2: (a) Side view and (b), (c) top views of the two surface terminations considered for Nb/manganese doping on the layered $LiNiO_2$ (101) surface. 62
Figure 4.3: Total density of states for Nb/Mn-doped and pristine surfaces for $LiNiO_2$ (101) surfaces. 65
Figure 4.4: (a) EC molecule, (b) EC adsorbed on pristine sites, (c) EC adsorbed on Nb-doped, (d) EC adsorbed on Mn-doped on $LiNiO_2$ (101) surface on Ni site. 68

List of Tables

Table 1.1: Structural properties of layered $LiNiO_2$. 9
Table 1.2: Fractional Co-ordinates of layered $LiNiO_2$. 10

Table 3.1: Bulk $LiNiO_2$ lattice parameters (a, b, c), volume (V), interatomic distances and (d), heats of formation (ΔH_f). 48
Table 3.2: Elastic constant of the bulk $LiNiO_2$ structure for 0.001 strain. 50
Table 3.3: Elastic moduli and Pugh's ratio for 0.001 strains. 51

Figure 4.1 Shows the directions of different terminations cleaved (a) (101) surface, (b) (001) surface, (c) (100) surface, (d) (011) surface, (e) (110) surface, (f) (010) surface and (g) (111) surface of $LiNiO_2$. 60
Figure 4.2: (a) Side view and (b), (c) top views of the two surface terminations considered for Nb/Mn doping on the layered $LiNiO_2$ (101) surface. 62
Figure 4.3: Total density of states for Nb/Mn-doped and pristine surfaces for $LiNiO_2$ (101) surfaces. 65
Figure 4.4: (a) EC molecule, (b) EC adsorbed on pristine sites, (c) EC adsorbed on Nb-doped, (d) EC adsorbed on Mn-doped on $LiNiO_2$ (101) surface on Ni site. 68

List of Abbreviations

LIBs	Lithium-ion Batteries
EVs	Electric Vehicles
HEVs	Hybrid Electric Vehicles
TM	Transition Metals
EES	Electrochemical Energy Storage
BMS	Battery Management System
DOD	Discharge/Charge
SOC	State of Charge
SOE	State of Energy
NCM	Nickel Cobalt Manganese
$LiNiO_2$	Lithium Nickel Oxide
$LiCoO_2$	Lithium Cobalt Oxide
Nb	Niobium
F	Fluorine
SEI	Solid Electrolyte Interphase
EC	Ethylene Carbonate
DOS	Density of State
PPDOS	Partial Phonon Density of State
DFT	Density Functional Theory
PW	Plane-Wave
PAW	Projector-Augmented-Wave
LDA	Local Density Approximation
GGA	General Gradient Approximation

GEA	Gradient Expansion Approximation
PW91	Perdew-Wang 91
PBE	Perdew-Burke-Enzerhof
LAPW	Linear Augmented Plane-wave
VASP	Vienna Ab-initio Simulation Package
US-PP	ultra-soft Vanderbilt pseudopotent

CHAPTER 1

Introduction

Rechargeable batteries known as Lithium-ion batteries (LIBs) have high charge/discharge rates, extended lifespans, and require little maintenance [1, 2]. The life cycle of LIBs can be greater than 10,000 cycles depending on their depth of discharge/charge (DOD), producing energy densities of almost 250 $Whkg^{-1}$ [3, 4] . LIBs have become a leading choice for energy storage, widely utilized in power tools, consumer electronics, and electric vehicles (EVs) [5, 6] . Li-ions have a few advantages over other elements for rechargeable batteries. These benefits include a low ratio of charge to ionic radii, a high ion movement, and a low reduction potential. These characteristics allow the LIBs to provide comparatively high gravimetric and volumetric capacities.

1.1 Background

Lithium-ion batteries have several safety issues, such as thermal runaway, which is drawing more attention from the scientific community. Thermal runaway at the cell level often triggers a series of events resulting in the formation of a short circuit. Due to the properties of lithium ions, the development of lithium dendrites and short circuits is a common occurrence in lithium-ion batteries [7]. It's crucial to create new low-cost cathode materials with outstanding stabilities since the cathode material of Li-ion batteries has a considerable impact on both their capacity and price [8, 9] . Since lithium nickel oxide ($LiNiO_2$) [10, 11] and $LiNi_xCo_yAl_zO_2$ [12, 13] have a larger available capacity, it has garnered a lot of interest as a potential cathode material for EVs.

Secondary batteries have undergone several advancements, evolving from traditional lead-acid batteries to nickel-metal hydride batteries, and ultimately to lithium-ion batteries [14, 15, 16] . When compared to other rechargeable battery chemistries, Li-ion batteries offer the best combination of energy density, lifetime, safety, and affordability. These favourable features are aided by the cathode, which is typically a layered lithium transition metal oxide capable of extremely reversible lithium removal and intercalation [17] . $LiNiO_2$ is a cathode material with a high capacity (greater than 200 mAh/g) and operating voltage of 4.4 V [18, 10] . When $LiNiO_2$ is charged at 4.4 V for the first time, oxygen is freed and Li^+ ions de-intercalate, resulting in irreversible Li_2O and electrochemically active NiO_2 [19] . The loss of oxygen and migration of transition metal (TM) ions because an irreversible redox reaction [20] , Doping [21] and coating [22] surface modification techniques could suppress irreversible oxygen redox, thus showing improved electrochemical performance and capacity retention. However, the interactions between the cathode and the coating, as well as the effect of doping on surface stability, remain a challenge. As a result, it is crucial to comprehend the impact of surface doping and coating while cycling, as well as their reactivity to the electrolyte content.

1.1.1 Description of Lithium-ion Batteries

Humanity's excessive dependence on fossil fuels has led to numerous problems and has contributed to the ongoing depletion of traditional energy sources [23] . The development of advanced electrochemical energy storage (EES) devices has received enormous research attention due to the growing need to utilize renewable energy sources (such as wind, solar, etc.). Several different energy storage devices have been created during the past few decades. Due to their high energy densities, LIBs are one of the most alluring energy storage technologies. However, the

chemical instability of the highly flammable organic solvents (such as alkyl carbonates) utilized in commercial Li-ion batteries could result in safety hazards in abusive circumstances (such as thermal runaway, explosion, combustion, etc.) [24]. Lithium-ion batteries are made of two electrodes: cathode, and anode. Ions travel from one electrode to the other while the battery is being charged or discharged, and electrons leave the battery via the electrical current. The exchange of ions between the two electrodes is analogous to the rhythmic process of inhaling and exhaling, as it allows the battery to charge and discharge.

When the battery generates current, electrons flow from the anode to the cathode through an external circuit. During recharging, a reverse current drives lithium ions from the cathode back into the anode, returning electrons to the anode. This process enhances the battery's capacity. The repeated charging and discharging process is known as a cycle [25] . During discharge, the anode undergoes oxidation, losing electrons, while the cathode undergoes reduction, gaining electrons. During charging, this process is reversed [26].

Recent studies have shown that nanoparticles possess excellent mechanical stability for long-term cycling and offer substantial storage capacity [27, 28, 29]. The notable advantages include the small particle size, which enhances rate capability by reducing electron diffusion distances, a high surface area that promotes lithium absorption for higher capacities, the ability of small particles to better accommodate crystalline expansion during lithiation, and the potential of nanomaterials to improve mechanical stability and electrical connectivity within a network [30, 31, 32]

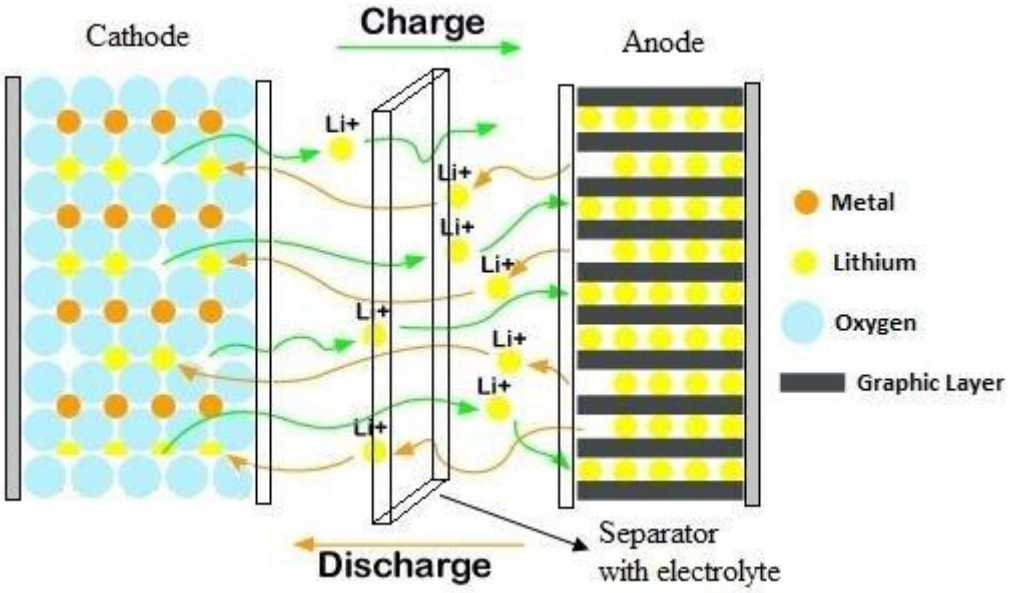

Figure 1.1: Charging and discharging phenomenon of Li-ion battery *[33]*

1.1.2 Details of a cell's/technical battery's components

Cell

A cell is the fundamental unit of a battery, typically generating a voltage output between 1 and 5 volts. It comprises three essential components: an anode, a cathode, and an electrolyte, which work together to enable EES and conversion.

Charging Process

Charging involves the input of electrical energy into a cell or battery, which is then converted and stored as chemical energy within the electrode materials.

Discharging Process

Discharging is the process in which the stored chemical energy is converted back into electrical energy to supply power to an external load or device.

Capacity

Battery capacity refers to the total amount of electric charge (measured in ampere-

hours, Ah) a cell can deliver during discharge at a given current density or C-rate. It is calculated as the product of the discharge current (in amperes) and the discharge duration (in hours), measured from a fully charged state down to the specified cut-off voltage.

Cycle Life

Cycle life indicates the number of complete charge-discharge cycles a battery can undergo before its capacity degrades significantly, typically defined as dropping below 80% of its initial rated capacity.

1.1.3 Applications

Lithium-ion batteries are widely used in energy storage applications, including portable devices, EVs, military defence, and space exploration, due to their lightweight nature, long lifespan, high energy density, and eco-friendly characteristics [34, 35, 36]. Precise estimation of state parameters is crucial for the safety of lithium-ion batteries and EVs, as well as for providing consumers with accurate battery information. Battery management systems (BMS) are essential for the operation of lithium-ion batteries, as they govern the battery's performance and safety. Two key metrics in BMS are the State-of-Charge (SOC) and State-of-Energy (SOE) [37, 38, 39] . Lithium-ion batteries have several advantages over other batteries, including their lightweight and electronegativity, which makes them the battery of choice [40]. Due to their security features, high output voltage, capacity, energy density, long cycle life, minimal memory effects, and low self-discharge rates, LIBs have become the leading power source for a variety of electronic devices, ranging from portable gadgets to large-scale systems [41].

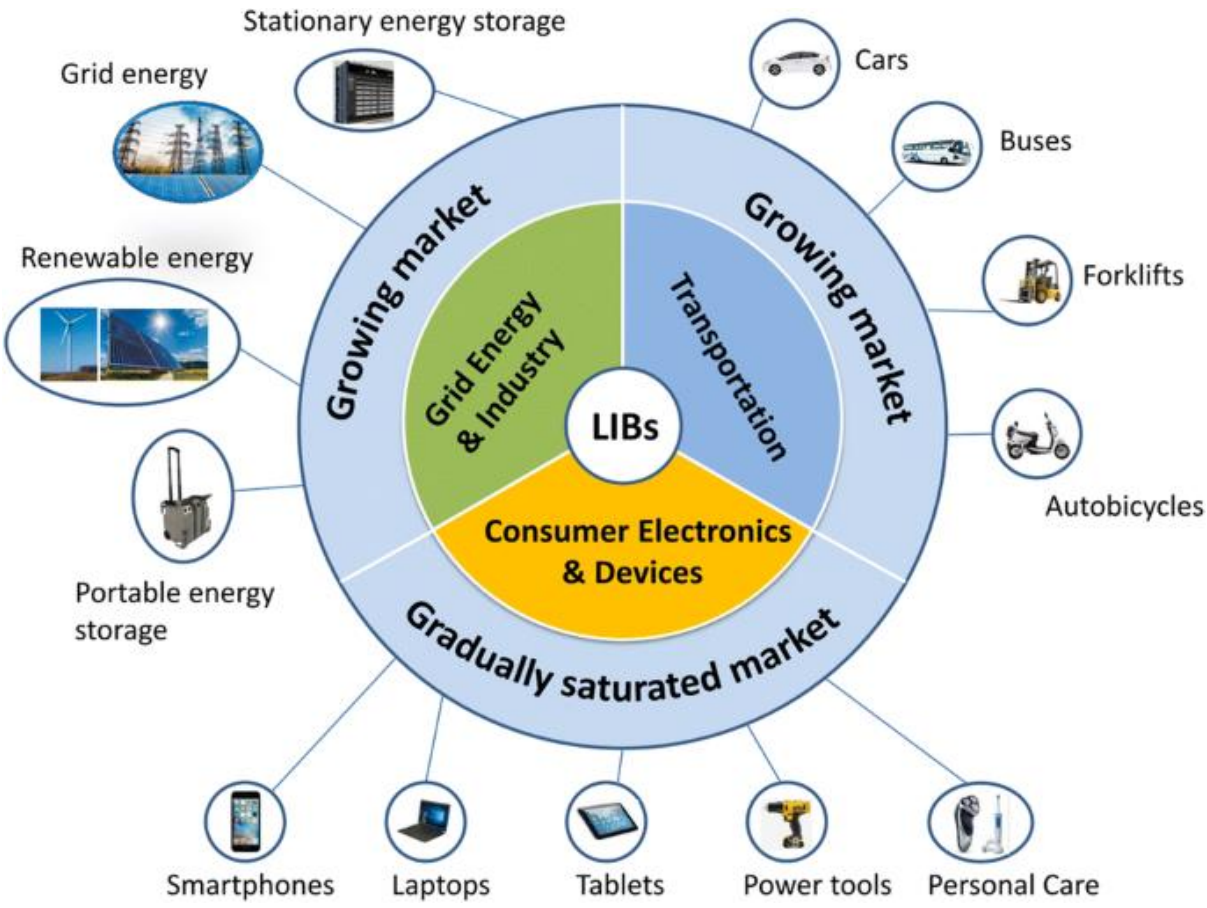

Figure 1.2: The various applications of lithium battery *[42]*.

1.2 Rational

Since the late 1970s, LIBs have been a primary subject of both industrial and academic research: the advanced battery technology's commercial success is undeniable, due to its high energy densities [43]. Lithium-ion batteries are popular due to their extended cycle life and resistance to memory effects. They serve as the primary power source for portable devices and also cater to large-scale applications, such as EVs and hybrid electric vehicles (HEVs) [44, 45, 46]. $LiNiO_2$ is considered one of the most ideal cathode materials for lithium-ion batteries [47]. Despite extensive research into various lithium-ion battery (LIB) cathode materials, layered oxides, particularly those based on $LiCoO_2$, $LiNiO_2$, and $LiMnO_4$, continue to be the industry standard. Researchers are actively exploring cobalt-free LIB cathode

materials to tackle problems related to cobalt's scarcity, high cost, and toxicity. $LiNiO_2$, a cobalt-free layered oxide with a comparable structure and a higher theoretical capacity than $LiCoO_2$, holds potential as a lithium-ion cathode material [48, 49, 50]. Due to its abundance and low cost, $LiNiO_2$ is considered one of the most promising cathode materials to replace $LiCoO_2$ [51]. To date, there has been a lot of focus on producing high-purity $LiNiO_2$ nanopowder using various synthetic processes [52, 53]. In respect to $LiNiO_2$ prepared in an O_2 atmosphere, it has been previously observed that preparing $LiNiO_2$ in an air environment helps reduce the cost [54].

Doping with bulk elements has been found to improve the structural stability of $LiNiO_2$ by altering the crystal lattice. This process helps prevent cation disorder and minimizes the formation of intergranular cracks in secondary particles. However, the impact of dopants on the stability of $LiNiO_2$ is largely influenced by the type and distribution of the dopants applied. When $LiNiO_2$ is charged, it significantly improves cycling stability. Notably, Niobium (Nb) has emerged as a promising dopant for various materials. This is due to the strong Nb-O bonding energy, which stabilizes lattice oxygen, and the relatively large ionic radius of Nb^{5+}, which expands the diffusion channels for Li+ ions. The benefits of significant Nb doping include stabilizing the layered structure, improving lithium diffusion kinetics, and reducing lattice expansion and contraction during cycling [55]. Fluorine (F) is another good substitute for O because it minimizes irreversible oxygen redox. At 3.0-4.6 V voltage, F substitution appears to increase the electrochemical performance of $LiNiO_2$ material [56]. Therefore, this study investigated the impact of surface doping on nickel and surface deposition on the primary surfaces of layered cathode materials, with the aim of enhancing their electrochemical stability and improving their interaction with the electrolyte.

1.3 Literature Review

1.3.1 Overview

This section provides a comprehensive review of the literature on various types of lithium-ion battery cathode materials, focusing on their structure, electrochemical properties (including capacity, cycle performance, and rate capability), synthesis methods, and potential strategies for enhancing both their structural and electrochemical characteristics. It specifically examines lithium-intercalating cathode materials, highlighting their pros and cons, along with the significant efforts to improve their overall performance. Based on their well-established crystal structures, these cathode materials are classified into three categories: layered metal oxides (e.g., lithium cobalt oxide ($LiCoO_2$), olivine ($LiFePO_4$), and spinel ($LiMn_2O_4$), as well as layered oxides like Li_2MnO_3-LMO_2 (where M can be Mn, Ni, or Co).

Lithium-ion batteries have been the focus of extensive research aimed at developing durable, affordable, and environmentally friendly energy storage solutions. The cathode is the most expensive component of a lithium-ion battery, making the development of efficient cathode materials vital, as it greatly influences both capacity and operating voltage [57]. Noteworthy cathode materials, such as $LiCoO_2$, $LiNiO_2$, $LiFePO_4$, $LiMn_2O_4$, and $LiMnO_2$, have been the primary focus of lithium-ion battery research [58, 59]. Recent research has investigated Li-Mn-O composite cathode materials to create cost-effective lithium-ion batteries. These materials leverage enhanced electrochemical properties and the greater abundance of manganese compared to nickel and cobalt [60, 61, 62], with 20 to 48% of manganese extraction in the Kalahari manganese district of South Africa.

The importance of nanostructured cathode materials has been widely studied as a promising method for achieving enhanced electrochemical performance in lithium-ion

batteries [63] . Computational methodologies, particularly atomistic potential-based approaches, have significantly influenced the electrochemistry of promising electrode materials [64] .Manganese stands as the 12th most prevalent element in the Earth's crust [65]**.**

1.3.2 Structural aspect of $LiNiO_2$

$LiNiO_2$ crystallizes in a layered monoclinic structure with the C2/m space group [49]. Table 1.1 below displays the physical properties of the material investigated in this study. It includes the lattice constants of the monoclinic structure, the symmetry of the space group, and the volumes of the system. A complete lattice parameter consists of three lattice constants. In three-dimensional space, lattices are defined by three constants: a, b, and c. for a monoclinic system, the lattice constants are such that a ≠ b ≠ c.

Additionally, Table 1.2 outlines the atoms present in the conventional unit cell of layered $LiNiO_2$.

Table 1.1: Structural properties of layered $LiNiO_2$.

Structure		**$LiNiO_2$**	**$LiNiO_2$**
Lattice constants (Å)	a	4.8984 [65]	5.005 [66]
	b	8.4496	8.670
	c	4.9692	5.016
Space group		C2/m	C2/m
		194.60	-
ΔH_f (kJ/mol)		-602.03 [67]	-619.00 [68]

Figure 1.3 below illustrates the positions of the lithium, nickel, and oxygen atoms, as described in Table 1.2. The table shows the atoms present in the standard unit cell of layered $LiNiO_2$. The second column lists the number of atoms of each type in the unit cell, along with their respective Wyckoff sites. In the monoclinic crystal structure of $LiNiO_2$, lithium, and nickel occupy the 2c and 4g sites, respectively, in the lithium/transition metal layers. Both lithium and nickel atoms are located within octahedra formed by oxygen atoms, which occupy the 4i and 8j sites. The stoichiometry of this structure is represented as $Li_6Ni_6O_{12}$, which simplifies the empirical formula $LiNiO_2$. The number of atoms in the unit cell corresponds to six times the number of atoms in the formula unit (Z = 6).

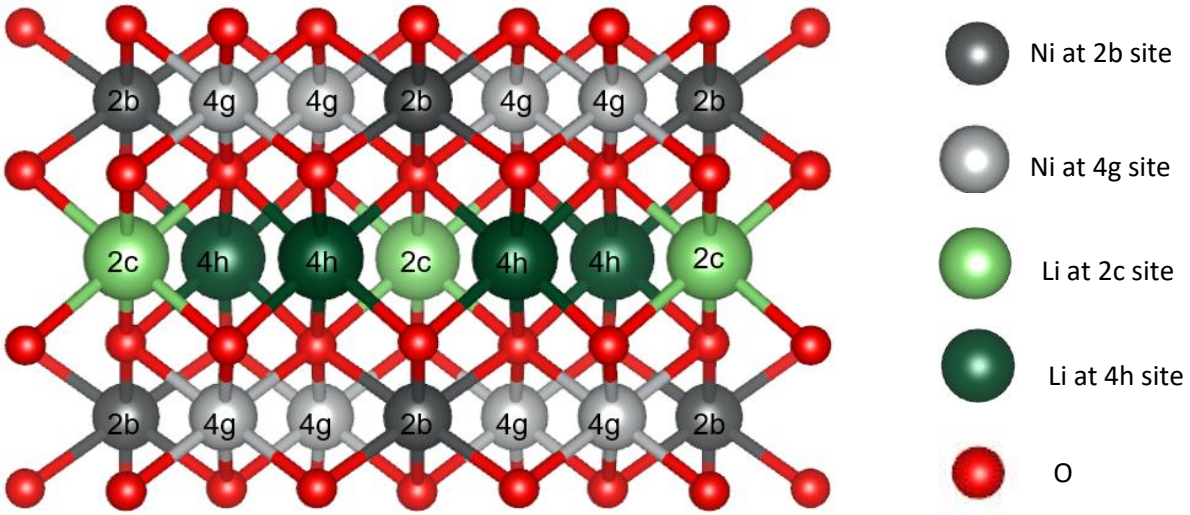

Figure 1.3: Crystal structure of layered $LiNiO_2$ and the atomic occupation positions of Li and Ni atoms.

Table 1.2: Fractional Co-ordinates of layered $LiNiO_2$.

Atoms	Positions	X	Y	Z
Li	2c	0.000	0.000	0.500
Li2	4h	0.000	0.666	0.500
Ni	4g	0.000	0.833	0.000
Ni2	2b	*0.000*	*0.500*	0.000

O	4i	*0.230*	*0.000*	*0.766*
O2	8j	*0.257*	*0.327*	*0.775*

1.3.3 Cathode Layered Material

Extensive research has been conducted on lithium-ion batteries to create a durable, affordable, and environmentally sustainable energy storage solution. A key focus has been the design of efficient cathode materials, which are essential for controlling the battery's capacity and working voltage. These cathode materials are currently recognized as the most expensive component of the battery [57]. The rechargeable lithium-ion battery is recognized as a crucial power source. Recent studies have shown that nanoparticles possess excellent mechanical stability over prolonged cycling periods and have significant storage capacity. The key advantages of nanoparticles include their small size, which improves rate capability by minimizing electron diffusion, offers a high surface area that may facilitate lithium absorption, leading to higher capacities, and allows small particles to better accommodate crystalline expansion during lithiation. Moreover, various nanomaterials can offer enhanced mechanical support and improve electrical connectivity within the network [69].

Modern cathode compositions commonly consist of NMC ($LiNi_xMn_yCo_zO_2$, x+y+z=1) compounds, which are TM oxides incorporating varying amounts of Co, Ni, and/or Mn. Recently, diverse substances have been under investigation for their suitability as secondary battery electrodes, including Li-Ni-Co-Mn-O, $LiCoO_2$ [70], $LiNiO_2$ [49], and $LiMnO_4$ [71]. Traditional TM oxides can operate at elevated potentials (4.3-5.0 V vs. Li/Li^+) to achieve greater electrochemical capacity per unit volume of active material. Despite considerable efforts to identify alternative layered oxides,

particularly those based on $LiCoO_2$ [72] . $LiCoO_2$ is a highly regarded cathode material known for its exceptional reversibility and rate capabilities.

However, its high cost and the inclusion of toxic cobalt present significant drawbacks. As a result, considerable efforts have been made to develop cathode materials that are more cost-effective and environmentally friendly than $LiCoO_2$. Among the promising alternatives is layered $LiNiO_2$, which, due to its lower cost and remarkable theoretical capacity of 275 mAh/g, it has emerged as a prominent candidate to replace $LiCoO_2$ in recent studies [73] . Extensive research emphasizes $LiNiO_2$ as a top cathode electrode material due to its high discharge capacity, higher operating voltage, improved energy density, cost-effectiveness, and environmental benefits when compared to $LiCoO_2$ [74, 75].

Many studies have focused on discovering alternative cathode materials that offer high capacities, function at higher voltages, and use cost-effective raw materials [76]. These materials demonstrate significant capacities within the high voltage range of 2.0 V to 4.8 V [77] . These materials have inherent disadvantages, including high reactivity with the electrolyte at elevated voltages, substantial initial irreversible capacity, capacity degradation during continuous cycling, and poor rate capability. [78].

1.3.4 Spinel $LiMn_2O_4$

There is a range of cathode materials available for LIBs, including $LiCoO_2$ [70] , $LiFePO_4$ [79] , $LiNi_{1-x-y}Co_xM_yO_2$ (M = Mn, Al) [80] , and $LiMn_2O_4$ [81, 82] . Each cathode material comes with its own trade-offs regarding factors such as energy density, cycle life, safety, cost, and other performance characteristics [83, 84] . Among these materials, spinel $LiMn_2O_4$ emerges as a promising option for lithium-ion

battery cathodes, particularly as a substitute for $LiCoO_2$, owing to advantages in safety, thermal stability, and cost-effectiveness [85] . While $LiMn_2O_4$ offers advantages like safety and affordability, its lower energy storage capacity and tendency to lose capacity over time limit its use in applications with high energy demands. This capacity fading is mainly caused by several factors that damage the material's structure during charging and discharging cycles. These factors include the Jahn-Teller distortion caused by Mn^{3+} ions, manganese dissolving from the cathode, and the breakdown of the electrolyte at high voltages [86, 87].

To overcome these challenges, several strategies have been developed, including controlling morphology, introducing cation doping, and applying surface coatings, all aimed at improving Li-ion storage performance. This involves enhancing the cycling stability of LMO [88, 89] . Implementing interface engineering by creating protective layers, such as CeO_2, ZnO, Al_2O_3, and MoO_3, on LMO (lithium manganese oxide) represents a promising strategy. This approach seeks to improve the structural and electrochemical stability of LMO by minimizing volume expansion, preventing manganese dissolution, and enhancing the diffusion of lithium ions and electrons during charging and discharging cycles [90, 91].

1.3.5 Layered $LiCoO_2$

LIBs are essential energy storage devices that power portable 3C (computer, communication, and consumer electronics) equipment, are widespread and indispensable [92, 93] . There is a growing demand for cathode materials that offer increased energy density, which has led to heightened interest in improving cathode performance. Since its commercialization by Sony in the 1990s, $LiCoO_2$ has maintained a vital position in the market and has garnered significant attention from

researchers. This is mainly due to its well-established industrial supply chain and high energy density [94, 95].

Most studies on LIBs that use $LiCoO_2$ and operate at approximately 4.53 V have already been brought to market. Typically, when the voltage exceeds 4.53 V, it leads to accelerated degradation of the electrodes and undesirable side reactions during higher voltage charging. This results in significant capacity loss. [96] . Several potential reasons for the degradation of $LiCoO_2$ include irreversible phase transitions, the formation of spinel phases, reduction of cobalt, loss of lattice oxygen, and cobalt dissolution caused by corrosion from hydrofluoric acid (HF), among other factors [97]. Previous research has shown that most degradation mechanisms take place at the electrode surface. As a result, coatings can help prevent side reactions between the electrode and the electrolyte. As a result, they can stabilize the interface between these two components [98].

Applying a thin metal oxide coating is one of the most efficient ways to improve the structural and chemical stability of the electrode/electrolyte interface. The impact of various metal oxide layers, such as MgO [99, 100], TiO_2 [101], Al_2O_3 [102] , has been studied. The impact of a $LiCoO_2$ electrode's electrochemical performance has been studied. Previous studies have demonstrated that metal ions from coating layers, such as Al^{3+} and Mg^{2+}, diffuse into the electrode lattice during the post-annealing process. This diffusion results in the creation of a solid solution at the interface between the coating layer and the electrode, improving electrochemical performance. The enhancement occurs by preventing electrolyte decomposition and reducing the dissolution of TM into the liquid electrolyte. Additionally, the coating layer helps

reinforce metal-oxygen bonds on the surface, minimizing structural changes [103, 104, 105].

1.3.6 Layered $LiNiO_2$

LIBs are regarded as the primary energy storage solution for the electric power grid, garnering significant attention in both energy storage systems and EVs [106, 107]. Cathodes play a crucial role in LIBs, greatly affecting their voltage and energy density. Initially, the market was dominated by lithium-ion batteries that used $LiCoO_2$ cathodes and graphite anodes [108]. However, the actual specific capacity of $LiCoO_2$ cathodes falls short of meeting the demands of high-energy batteries [109].

Therefore, there has been a continuous development of NCM materials [110, 111] and NCA materials [112, 113]. In recent years, with the extensive exploitation of cobalt resources due to LIBs development, cobalt has led to significant environmental pollution [114]. Hence, there is a shift towards developing cobalt-free cathode materials [115], along with a focus on green electrochemistry as the future trend [116]. In the quest for high energy density and cobalt-free batteries, researchers have turned their focus back to $LiNiO_2$ cathode materials [117, 118]. $LiNiO_2$ is recognized for its cost-effectiveness and high specific capacity. However, it also presents challenges, including an unstable structure and poor performance in terms of cycle life and C-rate. These issues are primarily due to the instability of trivalent nickel and substantial cation mixing between Li^+ and Ni^{2+} [119, 120, 4].

To address these issues, researchers commonly use techniques such as element doping or surface coating. For instance, doping $LiNiO_2$ with elements like Mn [121, 122], W [123], Mg [124], or Zr [125] enhances its cycle life and inhibits harmful phase transitions. Surface coating of materials can improve the properties of the

electrode/electrolyte interface and enhance the cyclic stability of cathode materials. For example, coating $LiNiO_2$ with substances such as ZrO_2 [126] or La_2O_3 [127], can enhance the cathode's cycle life. Moreover, some researchers have explored the design of core-shell structures [128] , this approach can improve the structural and chemical stability of cathode materials, although the material preparation process is complex.

1.3.7 Layered Surface Doping

Over the last decade, the demand for high-performance energy storage systems has surged, driven by the need for portable electronic devices and hybrid and EVs. These systems are required to provide high power and energy density, long lifespan, flexibility, and ensure safety [129] . At the same time, investigating alternatives to existing energy storage systems, like LIBs, is crucial for reducing the impacts of global warming and environmental damage caused by fossil fuel use [130, 131] . Batteries can be utilized on a large scale to effectively manage energy storage from reliable and renewable sources such as solar and wind [132].

$LiCoO_2$ is currently the most widely used cathode material in lithium batteries. However, its high cost and toxicity have sparked considerable interest in developing alternative cathode materials, such as $LiNiO_2$ [133] and $LiMn_2O_4$ [134] emerge as enticing alternatives. With a two-dimensional layered structure, it outperforms the three-dimensional spinel $LiMn_2O_4$ in terms of lithium ionic and electronic conductivities, layered $LiNiO_2$ exhibits greater potential for applications demanding high rates and high power [135].

The performance of cathode materials has been enhanced through the exploration of various methods and theories. Approaches like surface coating and doping have been employed to improve the structural stability and electrochemical performance of nickel-rich cathodes. To counter performance degradation and ensure structural stability, cation substitution, and structural doping have been recommended [135]. The stabilization process categorizes the impact of cation doping into two types: (i) doping with low-valent metals such as Mg, Cu, Al, etc. which may stabilize the valence of the Ni ion or create electrostatic repulsion [136, 137, 138], This could potentially minimize cation mixing and prevent the migration of Ni^{2+} ions from the transition-metal layer to the Li layer during electrochemical cycles. (ii) The stabilization process through high-valent metal doping, such as Ti, Mo, Nb, etc. [139, 140, 141], often demonstrates increased complexity.

Additionally, maintaining a certain charge balance can help reduce cation mixing. Anion doping provides several benefits, including the ability to preserve the material's full capacity without requiring the replacement of active elements. Anions such as F, N, Cl, and S, which have a radius similar to that of the O-ion, are considered suitable candidates for doping. Woo et al. [142], observed that electrochemical impedance spectroscopy and electron microscopy can effectively reduce the interfacial resistance between the cathode and electrolyte in Ni-rich materials through F^- substitution. F serves as a beneficial substitute for O as it minimizes irreversible oxygen redox. Within the voltage range of 3.0 to 4.6 V, F substitution appears to enhance the electrochemical performance of $LiNiO_2$ material [143]. Many researchers believe that F doping enhances the cell's performance by reducing the impedance for lithium diffusion and stabilizing the crystal structure,

thereby preventing the formation of oxygen vacancies during the initial charging process [144].

Kim et al. suggested that replacing Nb in $LiNi_{0.5}Mn_{1.5}O_4$ would create a surface-proximate domain layer rich in Mn^{3+}, greatly enhancing its electrochemical performance [145] . Incorporating Nb into NCM (nickel-cobalt-manganese) cathode materials can strengthen the host structure during charge and discharge cycles. This enhancement leads to improved cycling stability, as the bond energy of Nb-O is stronger than that of M-O (where, M represents nickel, cobalt, or manganese).

1.4 Objective

The objective of the study is to:

I. study mechanical, electronic, and elastic properties of $LiNiO_2$ bulk,
II. construct and calculate the surface stability of low Miller index (001), (010), (100), (110), (101), (011), and (111) surfaces for $LiNiO_2$,
III. model and study the effect of Nb and Mn doping on the first and second layer of $LiNiO_2$ major surfaces,
IV. model and study the adsorption of EC on clean $LiNiO_2$ and doped $LiNiO_2$ surfaces.

1.5 Research Questions

I. Which low-index $LiNiO_2$ surfaces are the most stable?
II. How does doping the $LiNiO_2$ surface with Nb or Mn affect surface stability and electronic structure?
III. What is the nature and strength of interaction between ethylene carbonate (EC) and both pristine and doped $LiNiO_2$ surfaces?

1.6 Justification for the Study

The development of cobalt-free and high-performance cathode materials is crucial for the sustainable growth of lithium-ion battery technology. While $LiNiO_2$ offers a high theoretical capacity and economic advantages, its practical application is hindered by poor structural and electrochemical stability. Surface doping and engineering have shown promise in addressing these issues. However, the atomic-level understanding of how dopants like Nb and Mn, and interactions with electrolyte components such as EC, influence the performance of $LiNiO_2$ surfaces remains incomplete. This study provides a computational investigation aimed at filling this knowledge gap. The findings are expected to contribute to the design of more stable, efficient, and cost-effective cathode materials by identifying optimal surface modifications that improve structural integrity and electrolyte compatibility.

1.7 Intention of the Study

Rechargeable batteries known as LIBs have high charge/discharge rates, extended lifespans, and require maintenance [1, 2]. The life cycle of LIBs can be greater than 10,000 cycles depending on their depth of DOD, producing energy densities of almost 250 $Whkg^{-1}$ [3, 4] . The layered $LiNiO_2$ is considered one of the most promising cathode materials for lithium-ion batteries due to its cost-effectiveness and high capacity [146]. However, due to the interactions between the cathode and the electrolyte, it suffers from capacity fading. These interactions typically lead to the formation of a solid electrolyte interphase (SEI) layer on the cathode surface. While the SEI layer can stabilize the electrode-electrolyte interface, its formation consumes lithium ions and electrolyte components, reducing available lithium ions for the battery's operation. Additionally, TM ions from the cathode, such as nickel, may dissolve into the electrolyte, and migrate to the anode, further compromising the

structural stability and electrochemical performance of the cathode. These factors contribute to capacity fading over repeated charge-discharge cycles [147].

Spin-polarized density functional theory (DFT) calculations with on-site Coulomb interactions and long-range dispersion corrections (DFT+U-D3(BJ)) were employed, as implemented in the VASP code. The objective of this study was to examine the stability of the bulk structure, assess the impact of Mn and Nb doping on the surface stability of $LiNiO_2$, and investigate the reactivity of the electrolyte component, ethylene carbonate (EC), on both the doped and pristine $LiNiO_2$ surfaces.

To assess bulk stability, four key properties were evaluated: structural, electronic, mechanical, and vibrational. The structural analysis involved calculating the heats of formation and equilibrium lattice parameters. Electronic properties were assessed by computing and plotting the density of states (DOS) and band structures. Mechanical stability was evaluated by calculating the elastic constants, moduli, anisotropy, and Pugh's ratio at a strain of 0.001. Vibrational properties were investigated by calculating and plotting the phonon dispersion and partial phonon density of states (PPDOS).

Seven low Miller index surfaces—(001), (010), (100), (110), (101), (011), and (111)—were cleaved from the fully optimized $LiNiO_2$ bulk structure using the METADISE code. The stability of these surfaces was evaluated by calculating their relaxed surface energies. The most stable surface, (101), was doped on the first and second layers with single Nb and Mn atoms at various Ni positions. The stability of these doped surfaces was assessed by calculating their surface free energies.

To investigate the reactivity of EC, the molecule was adsorbed on both the doped and pristine surfaces through Mn/Nb/Ni and Ni sites, respectively. Adsorption

energies were calculated to determine the strength and nature of interactions between EC and the surfaces.

1.8 Outline of the Study

Chapter One outlines the significance of the study, the challenges faced, the improvement strategies implemented to address these challenges, and the current state of lithium-ion batteries. It also provides an overview of the structural aspects of $LiNiO_2$ systems based on previous research and presents a guide on how the study will be conducted.

Chapter Two discusses the theoretical strategies and computational approaches that will be applied to analyse the $LiNiO_2$ systems. This chapter summarizes various methods, including DFT and plane-wave pseudopotential methods.

Chapter Three explains the bulk stability of $LiNiO_2$, focusing on its ground state covering the bulk structure's cut-off parameters and k-points, as well as topics such as elasticity, the DOS, band structures, formation energies, and phonon dispersions.

Chapter Four examines the surface construction and stacking sequences of the seven low Miller index surfaces: (001), (010), (100), (110), (101), (011), and (111). It includes a discussion on surface energies and explores the impact of doping on the stable facet surfaces through the calculation of surface-free energies. Additionally, we examine the interaction between EC electrolytes and both the doped and pristine stable surfaces, identifying the most favourable adsorption sites.

Chapter Five provides a comprehensive conclusion and offers several recommendations. We summarize the findings of the study and provide suggestions for future research.

CHAPTER 2

Theoretical Studies and Computational Methods

In this chapter, the computational methods and theoretical framework employed in the study are discussed. Advances in computing power have enabled the use of computational tools to describe key properties and behaviours of various materials for a wide range of applications [148] . Computational simulations are used to theoretically investigate material properties such as structural, elastic, mechanical, vibrational, electronic, and surface characteristics. This modelling approach, which represents physical systems through simplified models, is widely applied in solid-state physics, chemistry, and materials science to predict real-world phenomena. All calculations in this study were performed using first-principles quantum mechanical DFT [149] to analyse and predict the properties of $LiNiO_2$. The DFT approach utilises the plane-wave (PW) and projector-augmented-wave (PAW) pseudopotential methods to solve the Schrödinger equation. Full geometry optimization of the structures was conducted using these methods to ensure accurate predictions of the material's behaviour.

2.1 Density Functional Theory

Density functional theory (DFT) is a quantum mechanical approach employed to study the electronic structure of many-body systems, such as atoms, molecules, and condensed matter phase [150, 151]. It is a technique for roughly approximating the Schrödinger equation's many-body system solution. The two theorems created by Kohn and Hohenberg [152] form the foundation of DFT. The first theorem states that the ground-state electronic properties of a many-body system can be determined

from the electron density, which depends on three spatial dimensions. This serves as the foundation for a many-body system's approximation using the electron density. The second theorem demonstrates that the electron density, which minimizes the total energy functional, is the exact solution to the Schrödinger equation. Therefore, if the actual energy functional exists, the ground-state electron density can be obtained by minimizing the energy. Furthermore, once the ground-state electron density is known, all the system's parameters can be determined [153] . The Schrödinger equation, which is equivalent to the Kohn-Sham equation, is expressed as follows:

$$[-\frac{\hbar^2}{2m} + V_{eff}(r)]\,\psi i(r) = \varepsilon_i \psi_i(r), \qquad (2.1)$$

where, ψi is the wave function of electronic state i and ε_i is the Kohn-Sham eigenvalue and whereby:

$$V_{eff} = VC(r) + \mu_{xc}[\rho(r)]. \qquad (2.2)$$

Equations (2.1 and 2.2) are called the Kohn-Sham equations. In contrast, the Coulomb potential operator, VC and the exchange-correlation potential operator, μ_{xc}, depend on the specific electron distribution in the system under consideration. The Coulomb or electrostatic potential $VC(r)$ at point r is generated from the electric charges of all nuclei and electrons in the system. The wave functions that correlate to the electron density serve to indicate the ground-state electron density, which is equivalent to the system's minimal total energy. According to Walter Kohn and Lu Jeu Sham, the total energy functional is given as

$$E = \frac{1}{2}\sum_{occ}\varepsilon_i + U_{nm} - \frac{e^2}{2}\iint \frac{\rho(r)\rho(r')}{|r-r'|}drdr' + E_{xc}[\rho(r)] - \int \rho(r)\mu_{xc}dr. \qquad (2.3)$$

Where, $\rho(r)$ is the electronic charge distribution. One-electron densities are created from the total electron density derived from one-electron wave functions.

$$E = E(\rho). \qquad (2.4)$$

The Hartree-Fock theory is one of the most straightforward applications of the ab initio techniques that allowed computations of the electronic structure of solids [154]. These methods employ a single Slater determinant and an exact N-body wave function to model the wave function and energy of a many-body system in a stationary state. The Hartree-Fock approach provides the foundation for techniques that accurately describe the ground-state electronic properties of a many-body system [155]. The likelihood of detecting an electron in space can be thought of as the electron density, which is an important aspect of DFT. An area with a higher electron density has a higher chance of containing an electron. A four-dimensional grid space is used to characterize the scalar quantity known as the electron density, which is often determined via Fourier synthesis. The electron density is expressed as, at a point r in space.

$$\rho = \rho(r). \qquad (2.5)$$

Where, ‴ represents the electronic density. The electron density of a many-electron system can alternatively be expressed using a three-dimensional Fourier series, i.e.

$$\rho(x,y,z) = \frac{1}{V_{cell}} \sum_h \sum_k \sum_l F(hlk) e^{-2\pi i(hx+ky+lz)}, \qquad (2.6)$$

where, the structure factor, F(hkl), is shown. A physical system's total energy is made up of the contributions from its kinetic energy, Coulomb power, and exchange-correlation energy, which describes all of the many-body interactions of the atoms it contains. Thus, the overall equation is:

$$E = T_0 + U + E_{xc}, \qquad (2.7)$$

where, T_0 is the total kinetic energy of the system, U as classical Coulomb repulsion energy of the electrons, E_{xc} is the exchange correlation energy.

2.1.1 Approximation Methods

2.1.1.1 Local Density Approximation (LDA)

The goal of using approximation techniques is to describe the exchange-correlation energy as a function of energy density. The local LDA to the exchange-correlation functional in DFT are based on the electronic density at each point in space. According to LDA, the exchange-correlation energy at a location in a material where the charge density varies gradually can be compared to that of a locally uniform electron gas with the same charge density. This common approximation replaces the exchange-correlation energy density of an inhomogeneous system with that of an electron gas evaluated at the local density. It is based on two assumptions: first, the exchange and correlation effects are primarily confined to the region around point r, and second, these effects are not significantly affected by changes in the electron density in the surrounding area [156]. When these two conditions are satisfied, the volume element dr is treated as if it were surrounded by a constant electron density (r), matching the value of dr. The homogeneous density (ρ) determines the exchange correlation energy of the homogeneous electron gas $E_{XC}^{\text{hom}}(\rho_0)$, which density $\rho(r)$ substitutes for in inhomogeneous systems by:

$$E_{XC}^{LDA}(\rho(r)) = E_{XC}^{\text{hom}}(\rho_0)\big|_{\rho_0 = \rho(r)}. \qquad (2.8)$$

The following formula represents a LDA for the exchange-correlation energy for spin-unpolarized systems (where the functional depend solely on density):

$$E_{XC}^{LDA}[\rho] = \int p(r)\varepsilon_{XC}(\rho)dr, \quad (2.9)$$

And

$$\frac{\partial E_{XC}(\rho(r))}{\partial \rho(r)} = \frac{\partial [\rho(r)\varepsilon_{XC}(r)]}{\partial \rho(r)}, \quad (2.10)$$

Where, E_{XC} represents the exchange-correlation energy density and ρ represents the electronic density. The weakly perturbed electron gas is an example of a system with slowly varying densities, and this approximation is also effective for systems with highly inhomogeneous electron densities, like atoms and molecules. LDA is further explored when the exchange-correlation hole and pair correlation function are taken into account.

$$\rho_{Xc}^{LDA}(r_1, r_2) = \rho(r_1)[g^{\text{hom}}([\rho];| r_1 - r_2 |], \quad (2.11)$$

Where, $g^{\text{hom}}[\rho]$ is the homogeneous electron gas' integrated pair-correlation function for the coupling constant [157]. The exchange-correlation part of the pair-correlation function, which remains unchanged by the coupling constant integration, can be expressed as follows:

$$g_{xc}^{LDA}([\rho]; r_1, r_2) = 1 - \frac{9}{2}\left[\frac{\sin(k_F(r_1) | r_1 - r_2 |) - k_F(r_1) | r_1 - r_2 | \cos(k_F(r_1) | r_1 - r_2 |)}{(k_F(r_1) | r_1 - r_2 |)^3}\right]^2, \quad (2.12)$$

where, $k_F(r)$ is the local Fermi wave vector using the formula:

$$k_F(r) = \sqrt[3]{3}\,\rho(r)^{\frac{1}{3}}. \quad (2.13)$$

$E_{XC} = E_x + E_c$, where, E_x and E_c are the exchange energy and correlation energy, respectively, allows for a linear breakdown of the exchange-correlation energy into exchange and correlation terms. In the context of the homogeneous electron gas, the exchange term assumes an analytical form (HEG). Analytical knowledge exists on a HEG's exchange-energy density. The exchange energy in a system with inhomogeneous density is calculated by applying the HEG results at each point, yielding the expression used by LDA for exchange under the approximation [158]:

$$E^{LDA}[\rho] = -\frac{3}{4}\left(\frac{3}{\pi}\right)^{\frac{1}{3}} \int \rho(r)^{\frac{4}{3}} dr . \qquad (2.14)$$

This equation satisfies the required exchange scaling criteria. For the correlation portion of $g^{\text{hom}}[\rho]$ and $E_C^{LDA}[\rho]$ there are equivalent equations. Around the reference electron, the LDA xc-hole is spherical and is specified as:

$$\rho_{XC}^{LDA}(r_1, r_2) = \rho_{XC}(r_1, s), \qquad (2.15)$$

where, $s = |r_1 - r_2|$ and it also satisfies the sum rule.

$$\int \rho_{XC}^{LDA}(r_1, r_2) dr_2 = 4\pi \int_0^{\infty} \rho_{XC}^{LDA}(r_1, s) s^2 ds = -1 . \qquad (2.16)$$

No analytical formulas are available for the correlation energy of the HEG beyond the high- and low-density limits, which represent infinitely weak and infinitely strong correlation, respectively. The high-density limit of the correlation energy density for a HEG with density is [159]:

$$\varepsilon_c = A\ln(r_s) + B + r_s(C\ln(r_s) + D), \qquad (2.17)$$

And the low limit

$$\epsilon = \frac{1}{2} - \frac{g_0}{r_s} - \frac{g_1}{r_s^{\frac{3}{2}}} - \ldots\ldots\ldots , \qquad (2.18)$$

where the Wigner-Seitz radius is connected to the density by:

$$\frac{4}{3}\pi r_s^3 = \frac{1}{\rho} \qquad (2.19)$$

The development of more advanced exchange-correlation energy approximations, like generalized gradient approximations or hybrid functionals, relies on local-density approximations, as any approximation of the exchange-correlation functional must be able to reproduce the exact results of the homogeneous electron gas (HEG) for constant densities. Therefore, LDAs are often an integral component of these functionals.

2.1.1.2 General Gradient Approximation (GGA)

The generalized gradient approximation (GGA) is an alternative approach that improves the LDA by expanding the exchange-correlation functional to include terms involving the gradient of the electron density. The gradients track variations in electron density and can be utilized to get closer approximations of local densities. The weakly changing electron gas is the foundation for the majority of gradient developments [157]. The gradient expansion approximations (GEA), as they are also known, can be summed up as follows:

$$E_x^{GEA}[\rho] = E_x^{LDA}[\rho] + \beta \int \frac{(\nabla\rho)^2}{\rho^{\frac{4}{3}}} dr + \ldots \qquad (2.20)$$

$$E_C^{GEA}[\rho] = E_C^{LDA}[\rho] + C(\rho)\int \frac{(\nabla\rho)^2}{\rho^{\frac{4}{3}}}\, dr + \cdots \quad (2.21)$$

where, β is a constant and C(ρ) is a functional established by the response theory. Nevertheless, since the concentrations of molecules and individual atoms do not vary significantly over space, the GEA does not improve the LDA. The analysis of the xc-holes shows that, while the long-range behavior is worsened, the short-range behavior is enhanced [160]. The GGA, which has the following formula as its symbol, is the corresponding approximation for the GEA:

$$E_{xC} = E_x[\rho(r), \nabla\rho(r)]. \quad (2.22)$$

When compared to LDA results, this can achieve accuracy that is similar to the associated wavefunction. The Perdew-Wang 86 (PW86), Lee-Yang Parr (LYP), Perdew-Wang 91 (PW91), Perdew-Burke-Enzerhof (PBE), and Revised PBE are various parameterizations of the Generalized Gradient Approximation (GGA), while there is only one LDA, known as RPBE. Some of these parameterizations are derived entirely from first principles, while others are semi-empirical, incorporating experimental data such as atomization energy into their development. Due to Perdew and Yang [161, 160, 162], PW91 functionals are the most frequently used. However, the generalized correlated functional for the new generalized gradient approximation (GGA) takes the following form:

$$E_{XC}^{GGA} = \int d^3r f(\rho_\uparrow(r), \rho_\downarrow(r), \nabla\rho_\uparrow, \nabla\rho_\downarrow). \quad (2.23)$$

Studies have shown that the expression reduced LSD atomization errors by a factor of five [163]. The Becke GGA for exchange energy [164], Perdew's exchange-correlation GGAs [165], and Perdew and Wang [166, 167, 168] are the GGAs that are most frequently utilized. The GGA and LDA have the following correlation:

$$E_x^{GGA}\ [\rho\uparrow,\rho\downarrow] = E_x^{LDA} - \beta\int\Sigma\frac{\rho\sigma(r)^{\frac{4}{3}}}{1}\frac{x_\sigma^2}{+6\beta x\sigma sinh^{-1}x_\sigma}\,d^3r, \qquad (2.24)$$

where, E_x^{GEA}=$-C_{x\sigma}\Sigma\ \rho\sigma^{\frac{4}{3}}(r)^3(r)$, C_x=$\frac{3}{2}$ $(\frac{3}{4\pi})$, X_σ=$\frac{|\nabla\rho|}{\rho\sigma^{\frac{4}{3}}}$, σ denotes $\uparrow or \downarrow$ electron spin. To determine the proper exchange energy for a noble gas, β is a constant parameter. For electron gas with slowly variable density, the correlation functional proposed by Perdew and Wang [166] provided a reliable prediction of the correlation energy:

$$E_x^{GGA}\ [\rho\uparrow,\rho\downarrow] = \int(r)\varepsilon c\ (\rho\uparrow,\rho\downarrow)d3r + \int\frac{C_c|\nabla\rho(r)|^2}{d_e\phi\rho(r)^{\frac{4}{3}}}d^3r, \qquad (2.25)$$

where, d= $2^{\frac{1}{2}}$ $[(\frac{1+\zeta}{2})^{\frac{5}{3}}$ +$(\frac{1-\zeta}{2})^{\frac{5}{3}}]$, ϕ=0.1929$[\frac{C_c(\infty)}{C_c(\rho)}]$ $\frac{|\nabla\rho|}{\rho^{\frac{7}{6}}}$, ζ=$\frac{\rho\uparrow,\rho\downarrow}{\rho}$ & $C(\rho)$ is a rotational polynomial of the density that incorporates seven adjustable parameters. The PBE exchange functional, popularly known as the GGAPBE exchange-correlation, is addressed in the form that includes an explicit enhancement factor above the local exchange factor.

$$E_x^{PBE} = \int(r)\ \varepsilon_x^{LDA}\ [\rho(r)]\ FXC\ (\rho,\xi,s)\ dr, \qquad (2.26)$$

where, ρ is the local density, ξ is the relative spin polarization and s=$\frac{|\nabla\rho(r)|}{2kF\rho}$, is the dimensionless density gradient. The following improves the factor:

$$(sFx = (\frac{1}{k+\mu s^2}\ (k + s2\mu + s2k\mu))) \qquad (2.27)$$

where, μ=$(\frac{\pi^2}{3})$ =0.21951 with β = 0.066725. The correlation energy is:

$$E_c^{PBE}\ [\rho\uparrow,\rho\downarrow\ ]\ = \int(r)\ [\varepsilon_c^{PBE}\ (\rho,\zeta)\ + H(\rho,\zeta,t)]dr, \qquad (28)$$

with

$$H\ (\rho,\zeta,t) = \frac{e^2}{a_0}\gamma\phi3\times ln\left\{1+\frac{\beta}{\gamma}t^2\left[\frac{1+A^2}{1+At^2+A^2t^4}\right]\right\}, \qquad (2.28)$$

where, A=$\frac{\beta}{\gamma}$ $[e^{\mathrm{E}_c^{PBE}\frac{[\rho]}{\gamma\phi^3}}-1]^{-1}$, =$|\frac{\nabla(\mathrm{r})}{2\mathrm{ks}\rho}|$ is the dimensionless density gradient, ks=$(\frac{4\mathrm{kF}}{\pi})^{\frac{1}{2}}$is the TF screening wave number and $\phi(\zeta)$=[(1+$\zeta)^{\frac{2}{3}}$+(1−$\zeta)^{\frac{2}{3}}$] is the factor used for spin scaling. When uniformly scaled to the high-density limit, E_c^{GGA} Eggo tends to:

$$-\frac{e^2}{a_o}\int d3rn\gamma\phi 3\times l\left[1+\frac{1}{\frac{xs^2}{\phi^2}+(\frac{xs^2}{\phi^2})^2}\right], \qquad (2.29)$$

where, s=$\frac{|\nabla \mathrm{n}|}{2\mathrm{kFn}}$=$(\frac{r_s}{a_0})^{\frac{1}{2}}\phi t/c$ is another dimensionless density gradient.

2.2. Plane-wave pseudopotential methods.

The plane-wave pseudopotential method is a technique that precisely calculates the variation of self-consistent solutions. Its advancements have made it possible to predict the static and dynamic properties of molecules and crystalline solids [161]. The plane-wave pseudopotential method calculates the optimization of geometry, primarily the relaxation of internal parameters, and deals with the weak pseudopotential. Additionally, it is capable of simulating the electronic ground states of semiconductors, insulators, and metals.

2.2.1. Plane-Wave Basis Set

The above-described plane-wave approach is more accurate and effective at calculating a material's characteristics. It was created for tasks such as investigating the supercell technique for atoms and surfaces in periodic materials. The Bloch's theorem asserts that the eigenstates of a one-electron Hamiltonian can be expressed as a plane wave modulated by a function with the periodicity of the crystal lattice, $H=-\frac{\hbar^2\nabla^2}{2m}+V(r)$, where, V(r + T) = V(r) this approach is based on the principle that for all Bravais lattice translation vectors T, one can choose a plane

wave multiplied by a function that has the periodicity of the Bravais lattice. This theorem facilitates the expansion of electronic wave functions into a discrete set of plane waves, as shown below:

$$\psi_i = e^{[ik.r]} F_i(r). \qquad (2.30)$$

This expression consists of a wave-like component and a cell-periodic part, where,

$$F_i(r) = \Sigma_G \rightarrow C_{i,G} e^{[iGr]}, \qquad (2.31)$$

where, G denotes the periodic cell's reciprocal lattice vectors. Each unique electrical wavefunction ψki(r) is denoted by:

$$\psi k_i(r) = \sum_G \rightarrow C_{i,k+G} e^{[i(k+G).r]}, \qquad (2.32)$$

where, $C_{i,K+G}$ are the plane wave coefficients, they completely depend on the kinetic energy, $(\frac{\hbar^2}{2m})\ |K+Gc|^2$, and the plane waves with high kinetic energy are less significant than those with low kinetic energy. The following formulas can be used to compute the cut-off energy on a finite basis:

$$(\frac{\hbar^2}{2m})\ |K + G_c|^2 < E_{cut}. \qquad (2.33)$$

When its total energy converges to the requisite accuracy, the cut-off is chosen by progressively increasing its magnitude [169] . However, as the number of plane waves grows, it becomes possible to characterize the changing characteristics of the achieved infinitely large number of basis sets more quickly. In summary, the discrete plane-wave basis set is applied with a finite cut-off energy to create the finite basis set. The cut-off energy should be increased until full convergence is achieved, notwithstanding the possibility that doing so will cause computational mistakes. To

cut down on errors and guarantee good convergence, one should additionally employ a denser set of k-points.

2.2.2. Pseudopotentials

The pseudopotential is a hypothesis that seeks to make calculating energy density less challenging. The theory is set up so that the genuine wavefunction and potential agree well outside of some cut-off radius E_{cut} and the pseudo wavefunction does not contain any abrupt nodes within the core regions. Additionally, the pseudopotential needs to maintain the element's characteristics, such as the phase shifts that result from scattering across the core, which typically rely on angular momentum. Due to the low reactivity of the 42 core electrons, this theory replaces the Coulomb potential of the core electrons and nucleus with a potential that acts on the valence electrons.

The wavefunctions of the core electrons, which are localized around the nucleus, exhibit minimal overlap with the core electrons of neighboring atoms. As a result, the strong Coulomb potential causes the core wavefunctions of an atom to fluctuate quickly. The distribution of the atom's core electrons is constant regardless of its chemical surroundings. This is advantageous since it requires less processing of the electrons and calculation of Kohn-Sham eigenstates. However, by leaving out the core electrons from the calculations, the overall energy is significantly reduced, making the calculations of the energy differences across atomic structures considerably more numerically stable.

The pseudopotential approximation was developed to simplify the complex, unresolved effects caused by the movement of core electrons and their interactions with the effective potential [170, 171] , the pseudopotential approximation was introduced. The schematic illustration in Figure 2.1 gives a more detailed explanation

of the pseudopotential's characteristics. The intense ionic potential causes the valence wavefunctions to oscillate quickly in the area where the core electrons are located. As a result, these oscillations keep the valence and core electrons in orthogonal relationship. The pseudopotential should generally be non-local and devoid of any projectors for various angular momentum states. The pseudopotential's generic formulation is as follows:

$$V_{ions} = \Sigma|lm > V_i < lm|lm, \qquad (2.34)$$

where, |lm| are the spherical harmonics and V_i is the angular momentum pseudopotential

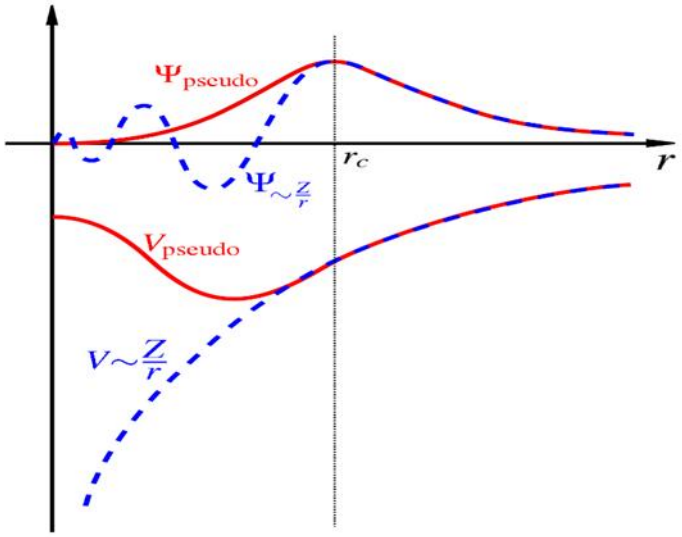

Figure 2.1: Schematic diagram for the illustration of an atomic all-electron wavefunction and the corresponding atomic pseudo wavefunction.

2.2.3. Projector Augmented Wave (PAW) Method

The wavefunction of materials exhibits distinct characteristics in various regions of space. The wavefunction oscillates quickly around the nucleus because of the strong attracting potential of the nucleus, whereas it is smooth in the region of bonding. When characterizing the bonding region accurately and taking into consideration the

significant differences in the atom centre, this is one of the limitations of the electronic structure technique. The wavefunction is composed of an envelope function outside the 44 atom-centered spheres and partial wave expansions inside them. This division is achieved through the augmented wave technique, where the envelope function and partial-wave expansions are matched with a term and its derivative at the sphere radius.

The projected augmented wave (PAW) method combines the linear augmented plane-wave (LAPW) technique with the formal simplicity of the conventional plane-wave approach [172]. The wavefunction can be expressed as follows:

$$\psi(r) = \widetilde{\psi}(r) + \sum_{\Lambda}\left[\phi_{\Lambda}(r) - \widetilde{\phi}_{\Lambda}(r)\right]\langle\tilde{p}_{\Lambda}|\tilde{\psi}\rangle, \qquad (2.35)$$

where, $|\psi\rangle$ and $|\tilde{\psi}\rangle$ stand for the wavefunction and the pseudo wavefunction, respectively, $|\phi\Lambda\rangle$ and $|\tilde{\phi}\ \Lambda\rangle$ for the isolated atoms, he one-electron Schrödinger equations and | for the pseudo-partial wave, respectively, and $\tilde{p}_{\Lambda}$ for the projector functions. In this formulation (as shown in equation 36), the outer envelope function and $|\psi\rangle$ act like an atom within an atom-centered sphere (interstitial region). The growth of $|\tilde{\phi}\ _{\Lambda}\rangle$ within the augmented region, which is done in a way that makes it equal to $|\phi_{\Lambda}\rangle$ interstitial regions, cancels out $|\tilde{\psi}\rangle$. While the core electrons are considered stationary in an atomic solution, the complete all-electron wavefunction is used, which relies on the total charge and spin density, including factors like the hyperfine interaction [173].

2.3. Implications In VASP

The Vienna Ab-initio Simulation Package (VASP) is a computer program designed for solid materials. It performs ab-initio quantum mechanical molecular dynamics using the projected augmented wave method, pseudopotentials, and a plane-wave

basis set. While the software is based on the DFT, it also incorporates hybrid functionals combining DFT, Hartree-Fock exchange, the many-body perturbation theory, and electronic corrections within the random phase approximation [174] . Effective matrix diagonalization techniques and Pulay/Broyden charge density mixing are used by VASP. While the original Car-Parrinello method, which integrates electronic and ionic equations of motion simultaneously, may have some limitations, this advanced methodology overcomes those issues. It also utilizes the PAW approach or the ultra-soft Vanderbilt pseudopotential (US-PP) [175] are used to characterize the interaction between ions and electrons. Ultra-soft pseudopotentials and projector-augmented waves offer a notable reduction in the number of plane waves per atom for TM and first-row elements. Using VASP, atoms can be relaxed to their local ground state by calculating forces and the complete stress tensor. Additionally, the VASP code is employed to compute the DOS. VASP is based on a program that was first created at MIT by M. Payne [160]. Thus, VASP split off from this root at a young age yet shares the same origins as the CASTEP/CETEP code.

Spin-polarized DFT calculations were carried out using the VASP [176] . All calculations were conducted using the Perdew, Burke, and Ernzerhof (PBE) exchange-correlation functional within the framework of the generalized gradient approximation (GGA) [177]. The Kohn-Sham (KS) valence state expansion's kinetic energy cut-off was set at 500 eV. All surfaces in the reciprocal space were integrated using a 4x4x1 k-point Monkhorst-Pack grid that was Γ-centred. In the application of Kresse and Joubert [161], the core electrons and their interactions with the valence electrons were represented using the projector augmented wave (PAW) method [172]. For nickel and oxygen, the core electrons consist of the 3s and 1s orbitals, respectively, while the valence electrons for lithium are applied to all of its orbitals.

Additionally, our calculations incorporated the semi-empirical Grimme method with the Becke-Johnson damping [D3-(BJ)] [178] for modeling long-range dispersion interactions, which are essential for accurately depicting surfaces [179] . During geometry improvements, gaussian smearing with a width of 0.05 eV was set to enhance the convergence of the Brillion zone integrations [178] . Accurate measurements of the electronic characteristics, magnetic properties, and total energies were made using the tetrahedron method with Blochl adjustments [180] . The Hubbard adjustment [172] the formulation of Dudarev et al. utilized this approach to improve the description of the localized 3d Ni electrons [181] . We selected the effective parameter U_{eff} = 6.0 eV, which is within the range of values mentioned in the literature [68].

2.4. Background of the Properties Studied

2.4.1. Geometry Optimization

Initially, we optimized the atomic positions and cell parameters, which is known as geometry optimization. This method additionally takes into account the inter-nuclear Coulomb energy in addition to the structural minimum. In the profile shown in Figure 2.2, the local and global minima are separated by a transitional state. One of the most challenging tasks in condensed matter physics is identifying the lowest energy path that atoms follow when transitioning from one stable configuration to another. The activation energy (Ea) is determined by calculating the total energy difference between the initial state and the saddle point, with the maximum energy along the minimum energy path representing this point. The energy difference between the final state and the initial state of the reaction also plays a key role in this process and beginning states can also be used to compute the activation energy (ΔE) of the reaction.

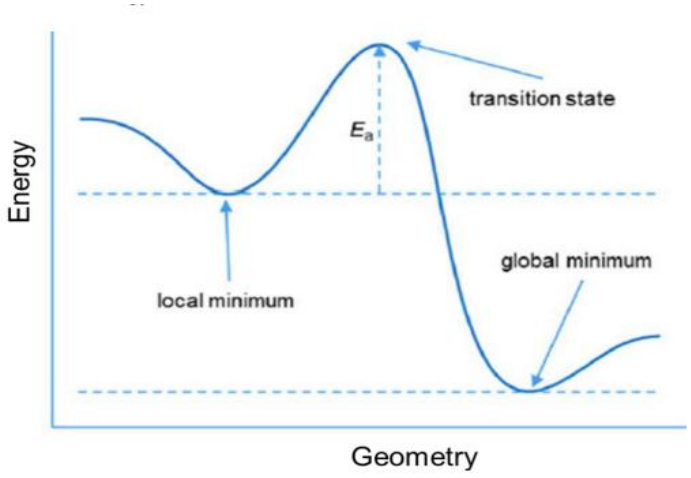

Figure 2.2: Representation of local and global minima with the transition state

2.4.2. Heats of Formation

The standard heat of formation of a material refers to the change in enthalpy when 1 mole of a substance is formed in its standard state. This can be determined using Hess's equation, which states that the standard enthalpy of a total reaction is the sum of the standard enthalpies of the individual reactions into which the overall reaction can be divided, forms the basis for the computation of the temperatures of formation [182]. The temperatures of formation and corresponding entropies offer a fundamental understanding of stabilities and the creation of phase diagrams. Estimates of the heat of formation (Hf) include:

$$\Delta H_f = E_c - \sum_i x_i E_i, \qquad (2.36)$$

where, E_c is the calculated total energy of the compound, E_i is the calculated total energy of the element i in the compound. The more stable the structures are, the lower their heats of formation. In Chapter 3, we will present the results of lattice parameters and heats of formation.

2.4.3 Elastic Properties

Elastic properties can be utilized as a stability requirement for structural transformations since they provide information about a material's resistance to externally applied strain [183, 184]. It may also be connected to several fundamental features of solid states, such as the equation of state and phonon dispersion spectra. Various theoretical and computational studies of homogeneous crystals' mechanical stability have been conducted [185] . Born began the methodical investigation of crystal stability under load. The Born stability criteria refer to a set of conditions on the elastic constants (C_{ij}) that are associated with the second-order change in the internal energy of a crystal during formation. However, Hill and Milstein suggested that the ranges of Born stability are highly sensitive to the coordinate system used, as the internal energy's convexity in a stressed crystal depends on the chosen coordinates [186].

According to Wang et al., the Born conditions are only relevant to the mechanical stability of unstressed systems and do not apply to stressed systems [187, 188] . Moreover, Barron and Klein noted that the conventional formulation of elastic constants derived from Helmholtz free energy cannot be directly applied to analyze the stress-strain relationship in a stressed state [189]. Nevertheless, it was shown by Wang and colleagues [188] that elastic constants cannot be used as stability criteria for a system under stress. They suggested that stability standards for isotropic stress be based on elastic stiffness coefficients. From path-dependent finite displacements, they were able to derive a more general expression for anisotropic stress.

The stability criteria are formally defined using elastic stiffness coefficients (C_{ij}), which govern the proper relationships between stress and strain under finite strain conditions. These coefficients account for both internal and external work involved

during the deformation process [189]. This suggests that the stability analysis mainly depends on a proper generalization of the zero-stress constants, applicable under any stress conditions. The shear modulus indicates the material's resistance to shape changes from shearing forces, while Young's modulus reflects its resistance to uniaxial tension.

The bulk modulus, on the other hand, measures the material's stiffness and the energy required for a given volume deformation, making it a crucial parameter in characterizing a material's physical properties [190]. The inverse of compressibility, the bulk modulus shows the bonding patterns in the material and is typically employed as a gauge for strength and hardness [191]. Pugh initially introduced the ratio of bulk to shear modulus (B/G) for polycrystalline phases, based on the assumption that the bulk modulus represents resistance to fracture, while the shear modulus represents resistance to plastic deformation. Low B/G values are linked to brittleness, while high B/G values are linked to ductility. The crucial value [192] separating brittleness and ductility is 1.75. A material's elastic constants, which are represented by its bulk modulus (B), shear modulus (C), young's modulus (E), poisson's ratio (υ), and shear anisotropy factor, determine how the material responds to an externally applied strain, or the stress required to sustain a particular deformation (A). For small deformations, it is envisaged that the crystal energy E will depend quadratically on the strain.

The type of material determines whether mechanical stability criteria apply. There are three tensile and three shear components in both stress and strain for each material, for a total of six components. The theory of elasticity necessitates a 66-symmetry matrix with 36 components to describe the relationship between stress and strain, so that for small stresses (σ) and strains (ε), $\sigma_1 = C_{ij}\varepsilon_j$ [193] . The

response of a material to externally imposed strain or the tension needed to maintain it is described by its elastic constants.

2.4.4 Phonon Dispersion

The optical properties of materials are determined by how the material interacts with electromagnetic radiation in the visible spectrum. There are numerous optical phenomena that are produced by photon interactions with a material's crystal structure. In the process of transferring photon energy to a medium, photons may be absorbed, transmitted, instantly released by the substance via reflection, or their velocities may change during transmission, leading to refraction. Band topologies vary amongst different materials. Non-metals have a variety of energy band topologies, while metals have partially full high-energy conduction bands. The stability of these materials is influenced by four optical phenomena: absorption, reflection, transmission, and refraction. To assess the stability of the spinel bulk structure, we computed and plotted the phonon dispersions using the PHONON code [194].

2.4.5 Density Of state

The DOS represents the number of available states at a particular energy level. It provides a thorough grasp of how molecules interact with solid surfaces and form chemical bonds. Within the Brillouin zone, each k-point corresponds to energy levels that collectively form energy bands, which can be visualized through a band diagram. A higher DOS at a specific energy level indicates more states are available for occupation, whereas zero DOS signifies the absence of states available for occupation at that energy level. The Fermi level (E_F) represents the energy level within the material's DOS and plays a crucial role in characterizing its electrical properties. In an insulator, E_F resides deep within a wide bandgap, far from any

states capable of carrying current. In a doped semiconductor, E_F is positioned close enough to a band edge to allow a small number of thermally excited carriers to exist. E_F is located within a delocalized band in a metal or semimetal. The volume that an ion takes up in a system can also be used to illustrate the DOS for that system's individual ions. The s, p, and d bands can also be used to represent it, this enables the analysis of the relative energies of different bands and their interactions with bonds.

2.4.6 Surface Calculations

Surfaces can be described by cleaving a bulk structure along different crystallographic planes, represented by Miller indices. The three integers h, k, and l are frequently used to denote the Miller indices, which are lattice planes. Based on the reciprocal lattice vectors, each index denotes an orthogonal plane to the direction and is denoted by the letters (h, k, l). For instance, the Miller indices (001) and (011) each indicate a plane that is orthogonal to the l direction and the k and l directions, respectively. Some indexed planes can be oriented perpendicular to the negative h, k, and l directions. For example, the plane $(00\bar{1})$ is perpendicular to the negative l direction.

Atoms on modeled surfaces generally have lower coordination compared to those in the bulk. Due to the presence of dangling bonds and changes in the coordination of surface atoms, the surface geometry tends to relax or, in some cases, reconstruct to allow the atoms to reach their equilibrium positions. The two most commonly used models for studying surface structures are the periodic and cluster models. The cluster model represents the surface as a small, isolated group of atoms, with one of the resulting facets maintaining the same symmetry and atomic arrangement as the studied crystal. In contrast, the periodic slab model creates exposed surfaces with a

vacuum on both sides of the slab. In this study, the slabs were derived from a fully optimized pristine bulk structure. The uppermost atomic layers may undergo relaxation, as shown in Figure 2.3, while the bottom atoms remain fixed to simulate the bulk structure. As a result, we gave the slabs with top atomic layers that could relax and those without fixed atomic layers the names relaxed surfaces and unrelaxed surfaces, respectively.

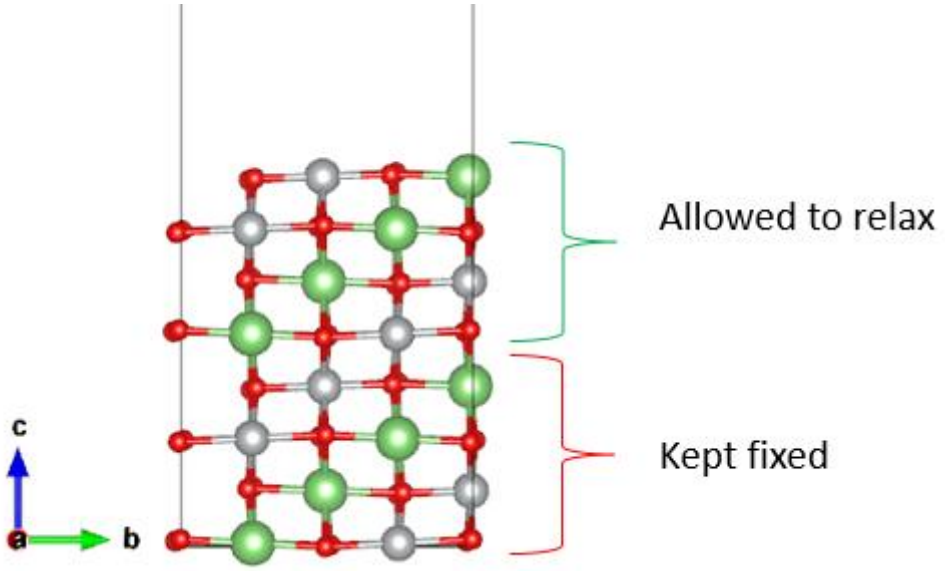

Figure 2.3: Representation of how the half-relaxed slab was calculated. The uppermost layers could relax while the lower surfaces were kept fixed at their relaxed bulk positions.

2.4.7 Surface Stability

The surface stability has an impact on the reactivity. More relativity toward adsorbing species is present at surfaces with lower surface stability. For the relaxed and unrelaxed slabs, surface energy of the simulated facets was computed. From static calculations, the unrelaxed surface energies (γ_u) were calculated as:

$$\gamma_u = \left(\frac{E_{u,slab} - E_{bulk}}{2A}\right), \qquad (2.37)$$

where, A is the slab's surface area, Eu is the slab's total energy (E_u), E_{bulk} is the slab's total energy (E_{bulk}), and E_{bulk} has the same number of formula units as the slab. After optimizing the geometry of half the slab, the two bottommost layers of the layered were fixed at their relaxed bulk positions, while the upper layers were allowed to relax freely, as shown in Figure 2.3 above. The relaxed surface energies (γ_r) for the spinel were also determined.

The relaxed and unrelaxed surfaces were present in the slabs; therefore, the surface energy was calculated as:

$$\gamma_u + \gamma_r = \left(\frac{E_r - E_{bulk}}{2A}\right), \qquad (2.38)$$

where, Er is the surface's overall energy at the halfway relaxed state.

CHAPTER 3

Convergence, mechanical, and vibrational properties of $LiNiO_2$ bulk phase.

In this chapter, we utilize DFT calculations to present and explain the structural characteristics of the bulk phase of $LiNiO_2$. We discuss the structural, mechanical, and vibrational aspects, accompanied by a benchmark convergence test. This convergence test, which examines kinetic cut-off energies and k-point meshes, identifies the minimum energy needed for structural convergence. Using the established convergence parameters, we conducted a geometry optimization and explored the resulting structural lattice parameters, heats of formation, and average interplanar distances of the Li/Ni-O bonds. We also investigated the mechanical properties, including elastic constants and moduli, as well as the electronic properties, such as the DOS and band structures. Additionally, we assessed the vibrational stability of the material through phonon dispersion curves. This chapter primarily focuses on the stability of the bulk structure and provides insights into the characteristics of the pristine layered $LiNiO_2$ structure.

3.1 METHOD

The bulk characteristics of $LiNiO_2$ were studied using density DFT calculations that were carried out using the VASP [176]. The computations were performed using the Perdew, Burke, and Ernzerhof (PBE) exchange correlation functional within the generalized gradient approximation (GGA) [177] . The projected augmented wave (PAW) formalism [172] as formulated by Kresse and Joubert [161] was employed to treat Li ($2s^1$), Mn ($3d^5 4s^2$), and O ($2s^2 2p^4$) as valence electrons and their interaction with the core electrons. A Hubbard correction [172] was used to improve the

description of the localized 3*d* Ni electrons in the formulation of Dudarev et al [181]. In line with the values stated in the literature, we utilized the effective parameter U_{eff} = 6.0 eV [195, 196, 197]. During geometry improvements, Gaussian smearing with a width of 0.05 eV was set to enhance the convergence of the Brillion zone integrations [178] . The Convergence was obtained using the conjugate-gradient approach. The convergence requirement was reached when the Hellmann-Feynman forces decreased below 0.02 eV/Å. Phonon code [198] was utilized to analyse the material's vibrational properties in the Materials Design module of the MedeA program of VASP.

3.2 Convergence test

To establish the proper cut-off energy of $LiNiO_2$ (with space group C2/m), the single point calculations varying the cut-off energies were conducted to deduce their total energy. The cut-off energy was adjusted between 100 and 900 eV with the increase of interval of 100 eV. The total energy was plotted as a function of the cut-off energy, as shown in Figure 3.1(a).). The kinetic energy cut-off from the plots was chosen when the graph began to show a minimal fluctuation in total energy. The curve for the $LiNiO_2$ bulk begins to show a negligible change at 500 eV. As a result, we consider the 500 eV as the minimum energy for subsequent calculations.

The Brillouin zone's ideal collection of special k-points was chosen using the Monkhorst-Pack technique of the k-points sampling to get the most accuracy out of the fewest available k-points. To indicate the minimum k-point mesh for the monoclinic $LiNiO_2$, we varied the k-points from 1×2×1 to 8×9×8 until the total energy change was negligible. The resulting k-mesh related to the total energy was plotted

as shown in Figure 3.1b below. The plot showed a minimal change around 7×8×7, which was the minimal k-mesh considered for further calculations.

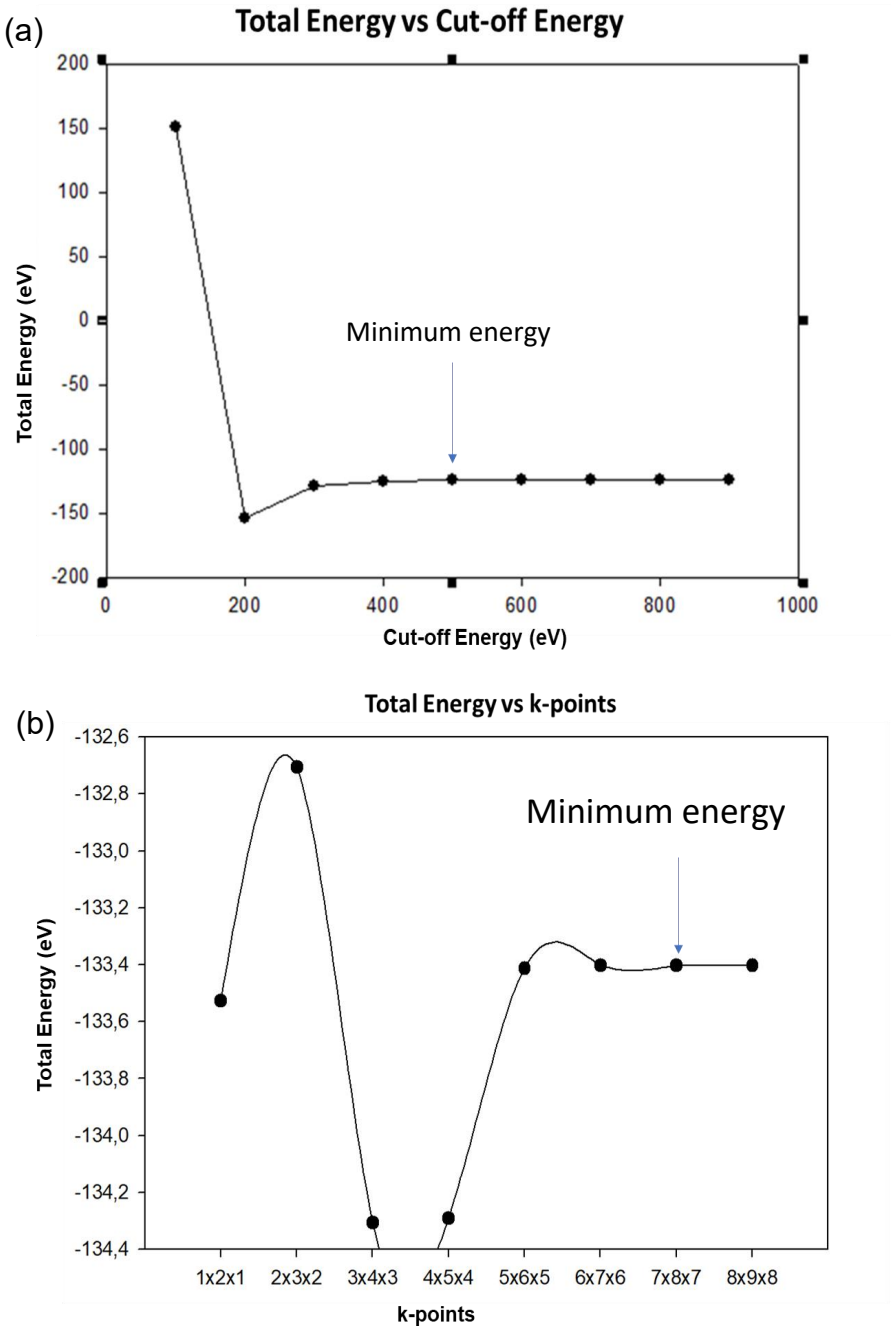

Figure 3.1: Graphs of total energy versus the (a) cut-off energy and (b) *k*-points of $LiNiO_2$.

3.3 Structural properties and heats of formation.

Table 3.1 presents the calculated lattice parameters, volume, bond length, and heats of formation for $LiNiO_2$ monoclinic. The calculated lattice parameters of a=4.888 Å, b=8.577 Å, and c=4.928 Å show a strong agreement with the experimental values (a=4.898 Å; b=8.450 Å; c=4.969 Å) [65]. We also observe that the calculated volume (209.368 Å³) closely matches the experimental value (194.600 Å³), with a difference of only 7.31%, indicating excellent agreement. The heat of formation (ΔHf), which represents the enthalpy change when one mole of a compound is formed from its elements in their stable states, plays a crucial role in assessing the structural stabilities of various crystal structures. The heat of formation is determined by subtracting the total energies of the individual elements from that of the compound. The formula for the heat of formation of $LiNiO_2$ is:

$$\Delta H_f(LiNiO_2) = {}^{1}/_{N}\,[E - (E_{Li} + E_{Ni} + 2E_O)], \qquad (3.1)$$

where, ΔH_f ($LiNiO_2$) is the total heat of formation of $LiNiO_2$, N is the total number of atoms, E is the total energy and E_{Li}, E_{Ni} and E_O are individual energies of Li, Ni and O respectively. The heat of formation is a fundamental thermodynamic quantity that provides insight into the stability of a compound. For $LiNiO_2$, the calculated heat of formation is −624.370 KJ/mol. The significantly negative heat of formation suggests that $LiNiO_2$ is thermodynamically stable. The heat of formation we calculated is in a good agreement with the experimental value -619.00 KJ/mol [68].

Table 3.1: Bulk $LiNiO_2$ lattice parameters (a, b, c), volume (V), interatomic distances and (d), heats of formation (ΔH_f).

Properties	$LiNiO_2$	$LiNiO_2$	$LiNiO_2$

Crystal structure	Monoclinic	Monoclinic	Monoclinic
a (Å)	4.888	4.898 [65]	5.005 [66]
b (Å)	8.577	8.450 [65]	8.670
c (Å)	4.928	4.969 [65]	5.016
V ($Å^3$)	209.368	194.600 [65]	-
d(Li−O) (Å)	1.982	1.939 [65]	-
d(Ni−O) (Å)	1.950	2.084 [65]	-
ΔH_f (KJ/mol)	-624.370	-619.000 [68]	-602.03 [67]

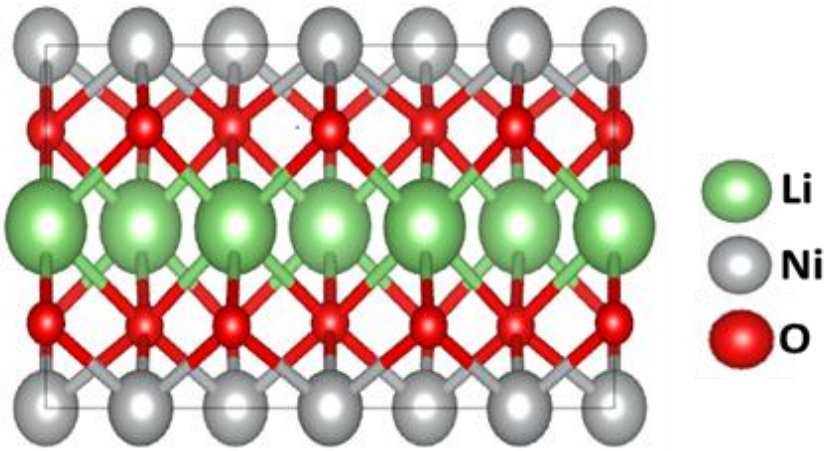

Figure 3.2: Crystal structure of monoclinic $LiNiO_2$.

3.4 Mechanical properties (Elastic Properties)

We discuss the mechanical properties of the bulk $LiNiO_2$ phase, calculated using a strain of 0.001. The elastic constants describe the system's rigidity in response to strain and provide a visual representation of the bonding interactions between atoms in the structure at equilibrium.

For monoclinic crystals, there are thirteen independent elastic constants (i.e. C_{ij} = C_{11}, C_{22}, C_{33}, C_{12}, C_{13}, C_{23}, C_{44}, C_{55}, C_{66}, C_{15}, C_{25}, C_{35}, C_{46}) and the estimated elastic constants are shown in Table 3.2. According to the monoclinic systems' mechanical stability criteria outlined in the literature [191] indicates that systems are mechanically stable when the following is satisfied:

$$\begin{aligned} &C_{ii} > 0 \ (i=1\text{-}6), \\ &[C_{11}+C_{22}+C_{33}+2(C_{12}+C_{13}+C_{23})]>0, \\ &C_{33}C_{55}–C^2_{35}>0, (C_{44}C_{66} -C^2_{46})>0, \text{ and} \\ &(C_{33}C_{22}\text{-}2C_{23})>0. \end{aligned} \qquad (3.2)$$

Negative elastic constants do not necessarily indicate instability within a crystal structure and do not directly impact the stability criteria for monoclinic materials. Instead, they reflect a particular type of deformation response. In monoclinic materials, these negative values often result from the material's anisotropic nature and the specific directions of the applied stress.

Table 3.2: Elastic constant of the bulk $LiNiO_2$ structure for 0.001 strain.

Elastic constant (GPa)	$LiNiO_2$
C_{11}	259.99
C_{12}	114.10
C_{13}	75.90
C_{15}	7.90
C_{22}	256.14
C_{23}	75.33
C_{25}	-11.16

C_{33}	212.99
C_{35}	-1.58
C_{44}	60.87
C_{46}	-17.15
C_{55}	62.52
C_{66}	68.87

The mechanical stability of $LiNiO_2$ is demonstrated through the calculated elastic constants, which satisfy the monoclinic stability criteria. Specifically, the calculated values for C_{11} and C_{44} are 259.99 GPa and 60.87 GPa, respectively, both of which are greater than zero. These confirms that the $LiNiO_2$ is mechanically stable. The degree of anisotropy in a material is then determined by calculating the anisotropy factor (A), when the value is less than or more than unity, an anisotropic solid, which has a value of 1, determines the degree of elastic anisotropy [192], the value is calculated using the following equation:

$$A = \frac{2C_{44}}{C_{11}-C_{12}} \tag{3.3}$$

The calculated anisotropy (A), shown in the table 3.3 below, is 0.83, which is less than 1, indicating that the bulk structures are elastically anisotropic materials.

Table 3.3: Elastic moduli and Pugh's ratio for 0.001 strains.

	Bulk (GPa)	Shear (GPa)	Young's (GPa)	Anisotropy	B/G
$LiNiO_2$	139.84	69.41	178.39	0.83	2.01

Additionally, we examined Pugh's ratio, which is the ratio of bulk modulus to shear modulus and is used to assess whether a material is brittle or ductile [199] . A material is considered ductile if the ratio of B/G is greater than 1.75, and brittle if it is less than 1.75. The B/G ratio of 2.01 is greater than 1.75, indicating that the structure is ductile.

3.5 Electronic properties (band structures and DOS)

The electronic properties (*i.e.,* band structures and DOS) are evaluated to describe the material's electronic arrangements in both conduction and valence band. The calculated band structures, as illustrated in Figure 3.2(a), reveal an overlap between the conduction band and the valence band at all Brillouin points. The spin-up electrons, represented by the red line, exhibit metallic characteristics, while the spin-down electrons, shown in blue, demonstrate semiconducting properties. The system has an indirect band gap of 0.708 eV, which is in reasonable agreement with the reported literature value of 0.460 eV [200]. Furthermore, the calculated total density of states (TDOS) indicates half-metallic behavior, with metallic characteristics for the up-spin electrons and semiconducting characteristics for the down-spin electrons, exhibiting a band gap of 0.708 eV.

(a)

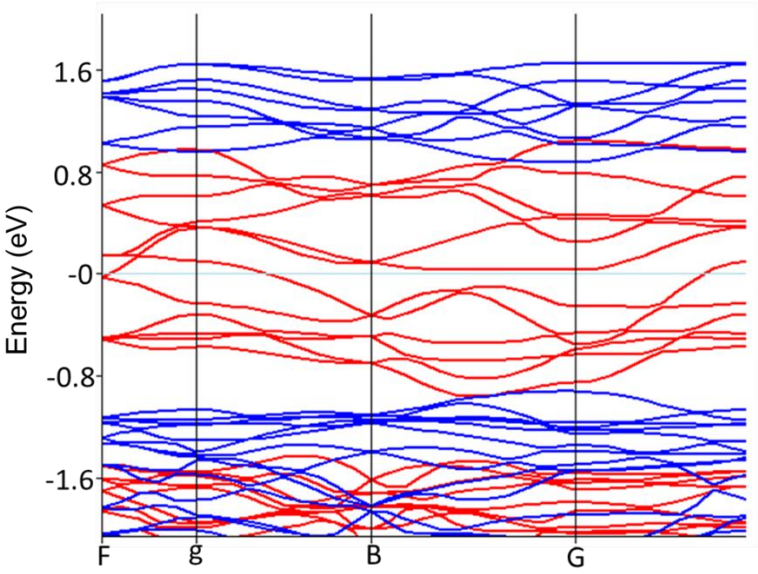

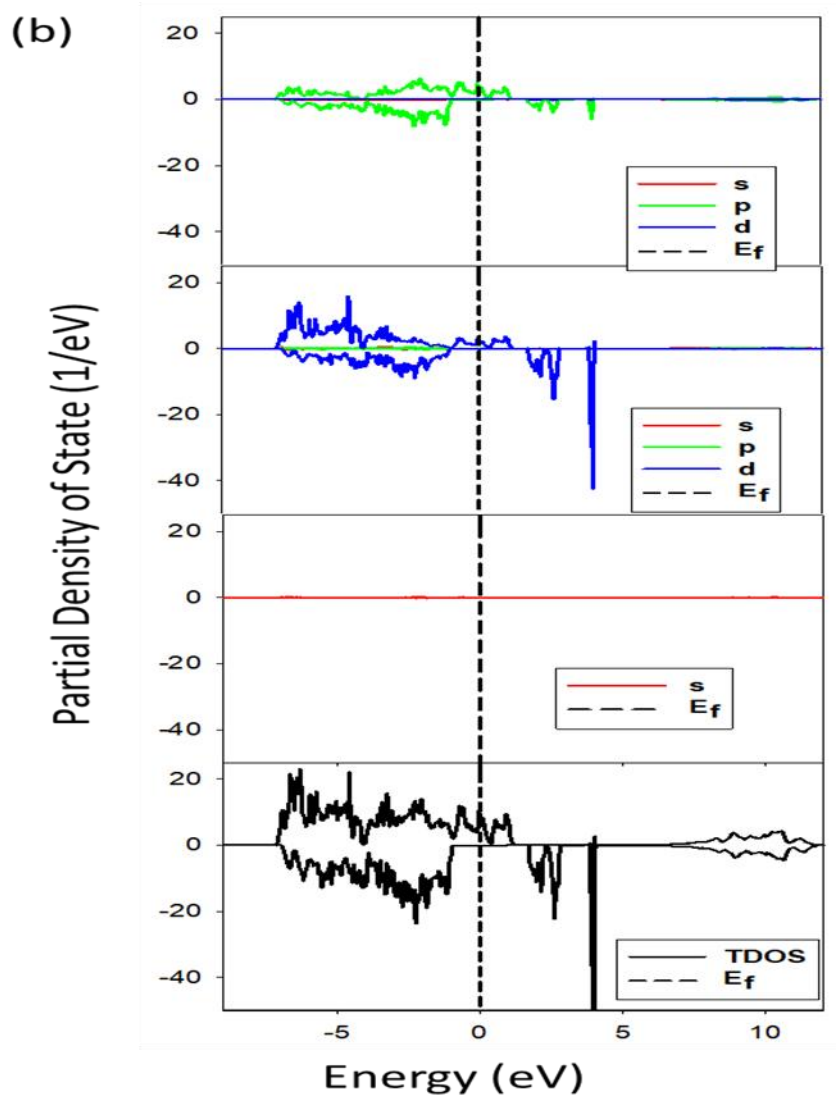

Figure 3.3: Electronic (a) band structure and (b) the DOS showing Li, Ni, and O contribution to the total DOS of $LiNiO_2$.

The TDOS in a half-metallic ferromagnetic system is spin-polarized, split into spin-up (↑) and spin-down (↓) components, and analysed within the energy range of -9 to 12 eV. To ensure consistency, the Fermi energy (Ef) is considered the system's highest occupied energy level. In the $LiNiO_2$ system, the Fermi level in the spin-up band overlaps the valence and conduction bands, indicating metallic behaviour. On the other hand, a small band gap around the Fermi level in the spin-down component suggests semiconducting behaviour with low electronic conductivity, as the Fermi

level lies within the band gap. The partial density of states (PDOS) is further examined to detail the spin-polarized electronic structure. From the PDOS curves, it is observed that Li contributes primarily through the 1s orbital, Ni through the 3d orbital, and O through the 2p orbital. The spin-up and spin-down bands are mainly formed by 3d-Ni and 2p-O states, with minor contributions from 1s-Li states. The 3d-Ni and 2p-O states dominate the spin-up and spin-down energy bands near the Fermi level, while the 1s-Li states appear around 7.0 eV in both spin-up and spin-down. These DOS results are consistent with the material's band structure.

3.6 Phonon Dispersion

Phonons are the quantum mechanical counterpart of a specific type of vibrational motion called normal modes in classical mechanics, where each component of a lattice oscillates at the same frequency. These normal modes represent the fundamental vibrations of the lattice. To examine the dynamic stability of the $LiNiO_2$ bulk structure, phonon dispersion curves were calculated in the ground state. Phonon calculations were performed using the PHON code, based on the small displacement method within the harmonic approximation [194] . The Phonon dispersion curves were plotted using the directions of the W, L, Γ, X, and K Brillouin zones as shown in Figure 3.4(a). The system appears to be dynamically unstable due to the negative vibrations observed in the gamma region of the Brillouin zone. According to the partial phonon density of states as shown in figure 3.4(b), the soft mode with negative frequency is attributed to the high vibration of oxygen atoms and minimal contributions from lithium in this frequency range. On the phonon dispersion curve, the acoustic band is located between -2.0 and -4.0 eV, while the optical band spans from -1.0 to 16.5 eV. Oxygen atoms dominate both the optical and acoustic bands, with lithium primarily contributing around 11.0 eV.

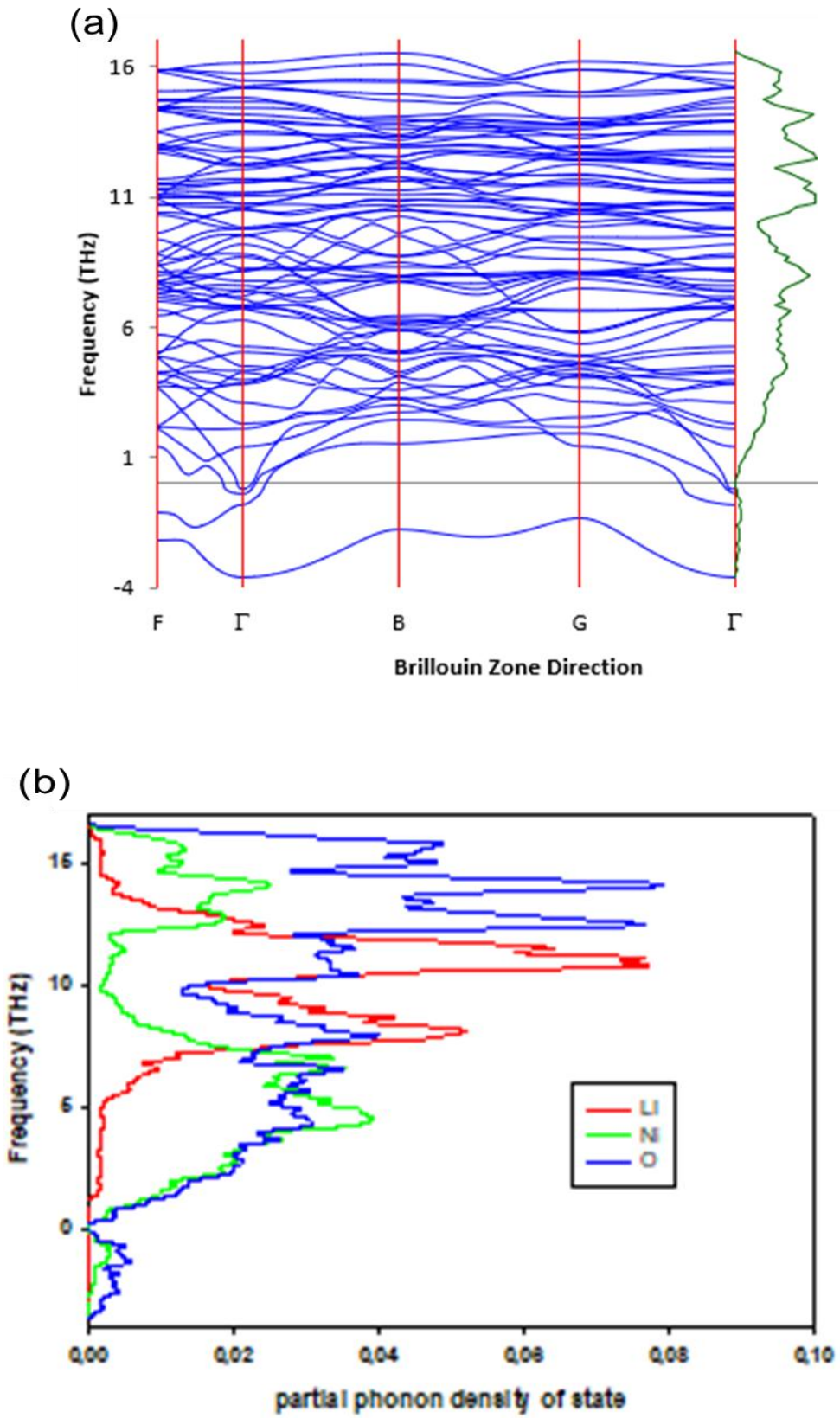

Figure 3.4: The plot of the (a) phonon dispersion curve and (b) partial phonon density of state.

3.7 Summary

In this chapter, DFT calculations were used to examine the structural characteristics, band structures, phonon dispersions, density of states, and elastic constants of $LiNiO_2$. The $LiNiO_2$ has a monoclinic structure with lattice parameters a = 4.888 Å, b = 8.577 Å, and c = 4.928 Å, which shows good agreement with the available data (a = 4.898 Å; b = 8.450 Å; c = 4.969 Å), with a discrepancy of only 2.4%. The electronic band structure revealed that the valence and conduction bands are separated by a small band gap of approximately 0.708 eV at the Fermi level, with electron overlap around the Fermi level. This demonstrated the material's status as a half-metallic ferromagnetic. As part of our investigation, the DOS was also investigated, which revealed the band gap of 0.708 eV at the Fermi level in the spin down, a sign that the substance is which confirms that the system is half-metallic ferromagnetic which aggress with the Band structure. The calculated elastic constants satisfy the stability criteria of monoclinic crystal. The structure is ductile because the calculated B/G ratio, which is greater than 1.75, was discovered to be 2.01. Since the calculated anisotropy (A) is less than 1, the bulk structures are expected to be elastically anisotropic. The structure appears to be dynamically unstable based on our plot of the phonon dispersion, which displays vibrations in the gamma region.

CHAPTER 4

4. Surface chemistry of $LiNiO_2$ and effect of organic electrolyte, ethylene carbonate

In this chapter, we employ spin-polarized DFT to explore the surface properties and the impact of Nb/Mn doping on the main surface of $LiNiO_2$. Seven low Miller index surfaces {i.e., (001), (010), (100), (110), (101), (011), and (111)} were constructed to initiate the analysis and then assess their stabilities by calculating the surface energies. Next, we examine the effect of Nb and manganese doping on the primary $LiNiO_2$ surface, considering doping on both the topmost and sub-surface layers (referred to as the first and second layers, respectively). Their stabilities are analysed by calculating surface free energies. Subsequently, Bader charge analysis for doped in relation to the pristine surfaces. The interaction between EC electrolytes and both doped and pristine $LiNiO_2$ surfaces (specifically the top layer) was examined.

4.1 Method

Spin-polarized DFT calculations were conducted using the VASP to model the surface layered [176]. All calculations were performed using the Perdew, Burke, and Ernzerhof (PBE) exchange-correlation functional within the framework of the generalized gradient approximation (GGA) [177]. The Kohn-Sham (KS) valence state expansion was set with a fixed kinetic energy cutoff of 500 eV. For integrating all surfaces in reciprocal space, a 4×4×1 k-point Monkhorst-Pack grid with the Γ-center as the origin was used. This was based on the method developed by Kresse and Joubert [161] [161], The projector augmented wave (PAW) approach was used to

model the core electrons and their interactions with the valence electrons [172]. The core electrons include levels up to 3d for nickel and 1s for carbon and oxygen, while all electrons are treated as valence electrons for lithium and hydrogen. Additionally, our calculations employed Grimme's semi-empirical approach with Becke-Johnson damping [D3-(BJ)] [179, 178] to model long-range dispersion interactions essential for accurately representing surfaces, Gaussian smearing with a width of 0.05 eV was applied during geometry optimizations to improve the convergence of Brillouin zone integrations [178]. The tetrahedron method with Blöchl corrections was employed to obtain accurate electrical and magnetic properties, as well as total energy calculations [172] [172]. The Hubbard adjustment [172] was used to enhance the description of the localized 3*d* Ni electrons in the formulation of Dudarev et al [181]. We used an effective parameter of U_{eff} =6.0 eV, which is consistent with the range of values reported in the literature [195, 196, 197], with a smearing width of 0.05 eV, the Gaussian smearing for Brillouin-zone integration was applied.

4.2 Surfaces Model and Energies

All surfaces were modeled from a fully optimized bulk structure using the dipole method available in the METADISE software [191] . To model the bulk phase of $LiNiO_2$, the bottom atoms were fixed in their relaxed bulk positions, while the remaining atoms were relaxed to approximate the resulting slabs. These slabs were designed to match the bulk structure, containing 96 atoms (24 formula units) with 24 lithium atoms, 24 nickel atoms, and 48 oxygen atoms. The number of atomic layers (N_{layers}) and surface areas ($A_{surface}$) of the seven low Miller index surfaces are presented in the table below. To prevent interactions between periodic slabs, a vacuum region of approximately 15 Å was introduced perpendicular to each slab's

surface. Geometry optimizations were performed using the conjugate-gradient method, and convergence was achieved when the Hellmann-Feynman forces were below 0.01 eV/Å.

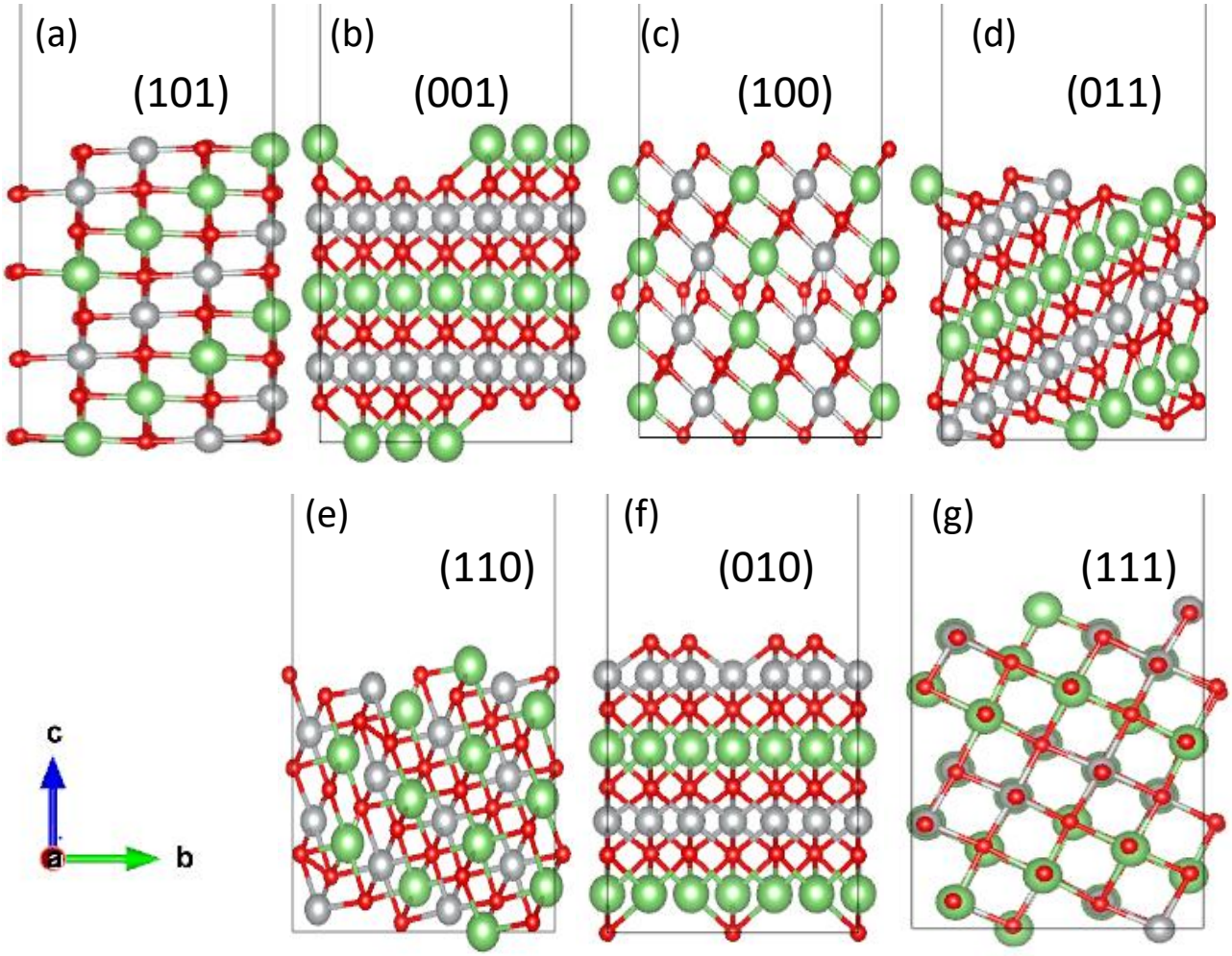

Figure 4.1 Shows the directions of different terminations cleaved (a) (101) surface, (b) (001) surface, (c) (100) surface, (d) (011) surface, (e) (110) surface, (f) (010) surface and (g) (111) surface of $LiNiO_2$.

The surface energy of the relaxed γ_r slabs was calculated to evaluate the surface terminations derived from the fully optimized bulk structure.

$$\gamma_r = \left(\frac{E_{u,slab} - E_{bulk}}{2A}\right), \qquad (4.1)$$

where, A is the slab's surface area, E_u is the slab's total energy (E_u), E_{bulk} is the slab's total energy (E_{bulk}), and E_{bulk} has the same number of formula units as the slab.

Table 4.1: Surface area ($A_{surface}$), number of layers (N_{layers}) and surface energies (γ_r), of each low Miller index $LiNiO_2$ surface.

Surface	Termination	N_{layers}	$A_{surface}$ (Å^2)	γ_r (eV/Å^2)
(001)	Li	9	83.858	0.129
(010)	O	9	91.315	1.608
(100)	O	9	84.552	0.212
(110)	Li	18	96.092	0.190
(111)	Li	12	72.114	0.453
(011)	O	18	95.482	0.211
(101)	Li-Ni-O	10	68.405	0.117

The seven $LiNiO_2$ surfaces with the lowest Miller index are listed in Table 4.1: summarizes their surface energies of the relaxed surfaces. The order of increasing surface energies, and consequently decreasing stability, is (101) < (001) < (110) < (011) < (100) < (111) < (010) and this pattern holds after relaxing as well. We also note that the Li-Ni-O-terminated (101) surface, with γ_r = 0.117 eV/ Å2 is the most stable surface.

4.3 Surface Free Energies

Here, we discuss the effect of surface doping with both Mn and Nb on the Ni atom(s) in the first and second layers, in order to examine the impact of surface doping, we

calculated the surface free energy for the changed surfaces, specifically for Nb and Mn-doped surfaces, using the following formula:

$$\sigma = \gamma_r + \frac{E_{LiNiMO_2} + E_{Ni_2} - E_{LiNiO_2} - E_M}{A}, \quad (4.2)$$

where, γ_r is the surface energy for the relaxed pristine $LiNiO_2$ surface, A is the area of the cell containing the surface slab, E_M is the energy of the M-doped $LiNiO_2$ surface, E_{LiNiO_2} is the energy of the relaxed pristine and M is Nb or Mn atom. A low positive value of σ indicates stability of the surface.

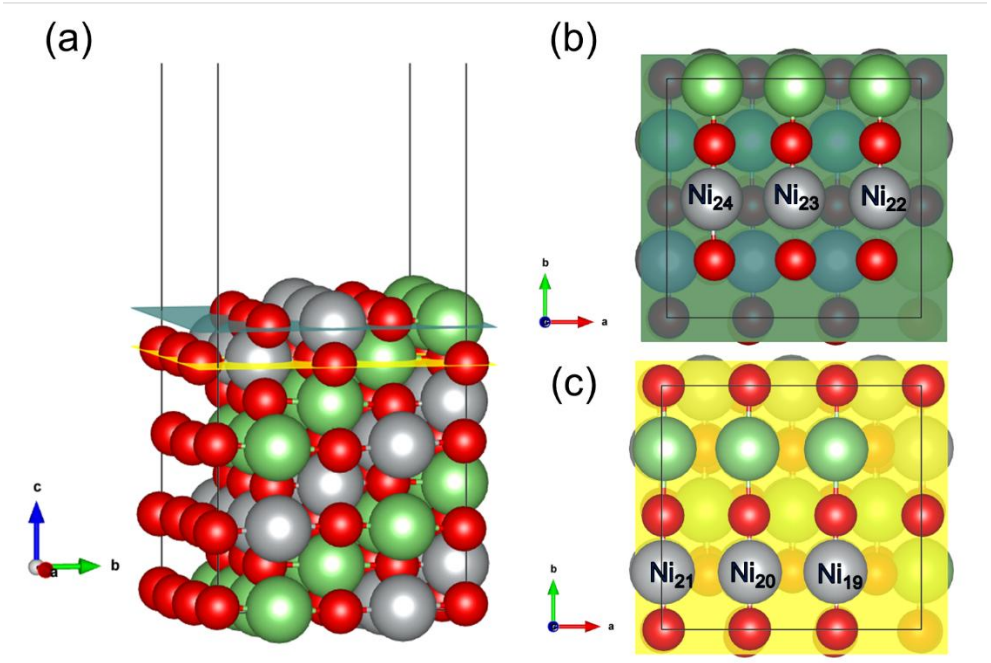

Figure 4.2: (a) Side view and (b), (c) top views of the two surface terminations considered for Nb/Mn doping on the layered $LiNiO_2$ (101) surface.

The surface free energies (σ) for single Nb and Mn-doped surfaces for the top and second layers are summarised in Table 4.2. The considered doping sites are indicated in Figure 4.2 for both top and second layers. Figure Upon single adsorption of both Nb and Mn atoms on the top layer of the $LiNiO_2$ surface, it was observed that

Ni_{22} was the most preferred with the lowest surface free energies of 0.057 and 0.093 eV/Å^2, respectively.

Table 4.2: Surface free energy (σ) for the single Nb and Mn doped on first and second layers of $LiNiO_2$.

Doping layers	Doping sites	σ_{Nb} (eV/Å²)	σ_{Mn} (eV/Å²)
first-layer	Ni_{22}	0.057	0.093
	Ni_{23}	0.067	0.094
	Ni_{24}	0.060	0.095
Sub-surface layer	Ni_{19}	0.041	0.097
	Ni_{20}	0.052	0.101
	Ni_{21}	0.063	0.111

The surface free energies (σ) for single Nb and Mn-doped surfaces for the first and second layers are summarised in Table 4.2. The considered doping sites are indicated in Figure 4.2 for both the first and second layers. Figure Upon single adsorption of both Nb and Mn atoms on the first layer of the $LiNiO_2$ surface, it was observed that Ni_{22} was the most preferred with the lowest surface free energies of 0.057 and 0.093 eV/Å^2, respectively. Similarly, a single Nb and Mn atom is doped on the second layer both preferred Ni_{19} with lower surface free energy of 0.041 and 0.097 eV/Å^2, respectively. As compared to the pristine (101) surface with γ_r = 0.117 eV/Å^2, the introduction of the Nb/Mn dopant generally stabilized the surface. Doping the surface with Nb enhances stability primarily in the second layer, whereas doping with Mn improves stability on the first layer.

4.4 Density of State

To investigate the structural and mechanical stability of the Nb/Mn-doped and pristine $LiNiO_2$ (101) surfaces, we analyze their total DOS plots in Figure 4.3. According to the literature, the DOS of structures with the same composition can be used to infer stability trends based on their behavior at the Fermi level (E_f). Structures with the highest DOS at E_f are generally considered the least stable, while those with the lowest DOS at E_f are deemed the most stable [201]. In the spin-up channel, the pristine surface exhibits a lower DOS near the Fermi level compared to the Nb- and Mn-doped surfaces, suggesting higher stability. In contrast, within the spin-down channel, the Nb-doped surface (with Nb positioned in the second layer) shows the lowest DOS, followed by the Mn-doped surface (with Mn located in the top layer). The absence of bands in the Nb-doped (top layer), Mn-doped (second layer), and pristine surfaces suggests that these materials exhibit half-metallic ferromagnetism. However, doping with Nb in the second atomic layer causes a notable shift in electronic properties. The DOS analysis reveals that Nb doping transforms the material into a fully metallic state, exhibiting metallic behavior in both the spin-up and spin-down channels. This change implies that Nb doping disrupts the original electronic structure, eliminating half-metallicity and improving conductivity across both spin channels. These results align with the predicted surface energy calculations.

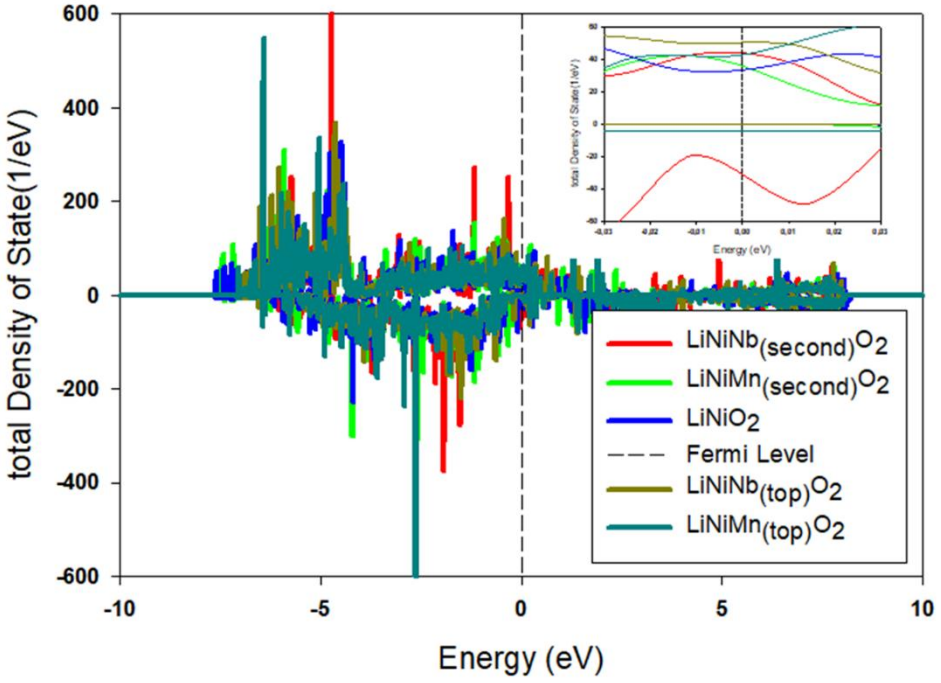

Figure 4.3: Total density of states for Nb/Mn-doped and pristine surfaces for $LiNiO_2$ (101) surfaces.

4.5 Work function and Bader Charges Analysis

The electronic charge transfer (Δq) analysis following Nb and Mn doping on $LiNiO_2$ surfaces, along with their corresponding work functions (ϕ), is shown in table 4.3. Bader charge analysis reveals that Nb holds higher charges in both layers, with values of 2.400 e^- in the first layer and 2.600 e^- in the second layer. This indicates that Nb acts as an electron acceptor, drawing electrons from neighboring Ni atoms. This electron withdrawal likely diminishes the reactivity of the Ni atoms, contributing to a more stable surface with reduced chemical activity. In contrast, Mn displays lower Bader charges than Nb, registering 1.700 e^- in the first layer and 1.800 e^- in the second layer, signifying that Mn is less efficient at electron withdrawal. This increases electron density around adjacent Ni atoms, potentially enhancing their reactivity and leading to a chemically more active surface. Additionally, the work

function, representing the energy required to remove an atom to the vacuum, was calculated using the equation:

$$\phi = E_{\mathrm{vac}} - E_{\mathrm{F}}, \quad (4.3)$$

where, E_{vac} and E_{F} are the surface electrostatic potential energy and the Fermi level, respectively.

Table 4.3: Bader charge analysis for the Nb/Mn doping (q(Nb/ Mn)) on the first and second layers of the $LiNiO_2$(101) surface alongside their neighbouring Ni atomic charges (q $(Ni)_{Neigb}$) and work functions (ϕ).

	Doping layers	q(Nb/ Mn) (e^-)	$q(Ni)_{Neigb}$ (e^-) Ni1	Ni2	ϕ (eV)
Nb-doping	1st layer	2.400	-0.216	-0.209	5.232
	2nd layer	2.600	-0.208	-0.113	5.281
Mn-doping	1st layer	1.700	-0.183	-0.171	5.222
	2nd layer	1.800	0.144	0.107	5.190

The Nb-doped surface has a higher work function (Φ) than the Mn-doped surface, with values of 5.232 eV for the first layer and 5.281 eV for the second layer, respectively. A higher work function generally corresponds to reduced surface reactivity. This decrease in work function implies that Mn-doped surfaces may exhibit increased reactivity.

4.6 Ethylene Carbonate Adsorption

We discuss the effects of the adsorption of electrolyte components, specifically EC, on the Nb/Mn-doped $LiNiO_2$ (101) surface compared to the pristine surface. Firstly,

we calculated the energy of the EC molecule, which was -61.974 eV. We examined the adsorption of EC on various nickel positions in the top layer of both doped and pristine surfaces. We then calculated the energy of EC adsorption on manganese (Mn)-doped and Nb-doped $LiNiO_2$ (101) surfaces, as well as on pristine $LiNiO_2$ (101) surfaces. The adsorption energy (E_{ad}) of an EC molecule on the $LiNiO_2$ (101) surface is defined as follows:

$$E_{ad} = E_{sys} - (E_{surf} + E_{EC}), \tag{4.4}$$

where, E_{sys} represent the total energy of the adsorption system, E_{surf} refers to the total energy of the $LiNiO_2$ (101) slab and E_{EC} corresponds to the total energy of an isolated EC molecule. The carbonyl oxygen of EC is coordinated to the Nb and Mn sites of the doped $LiNiO_2$ surface to build the adsorption surface structures.

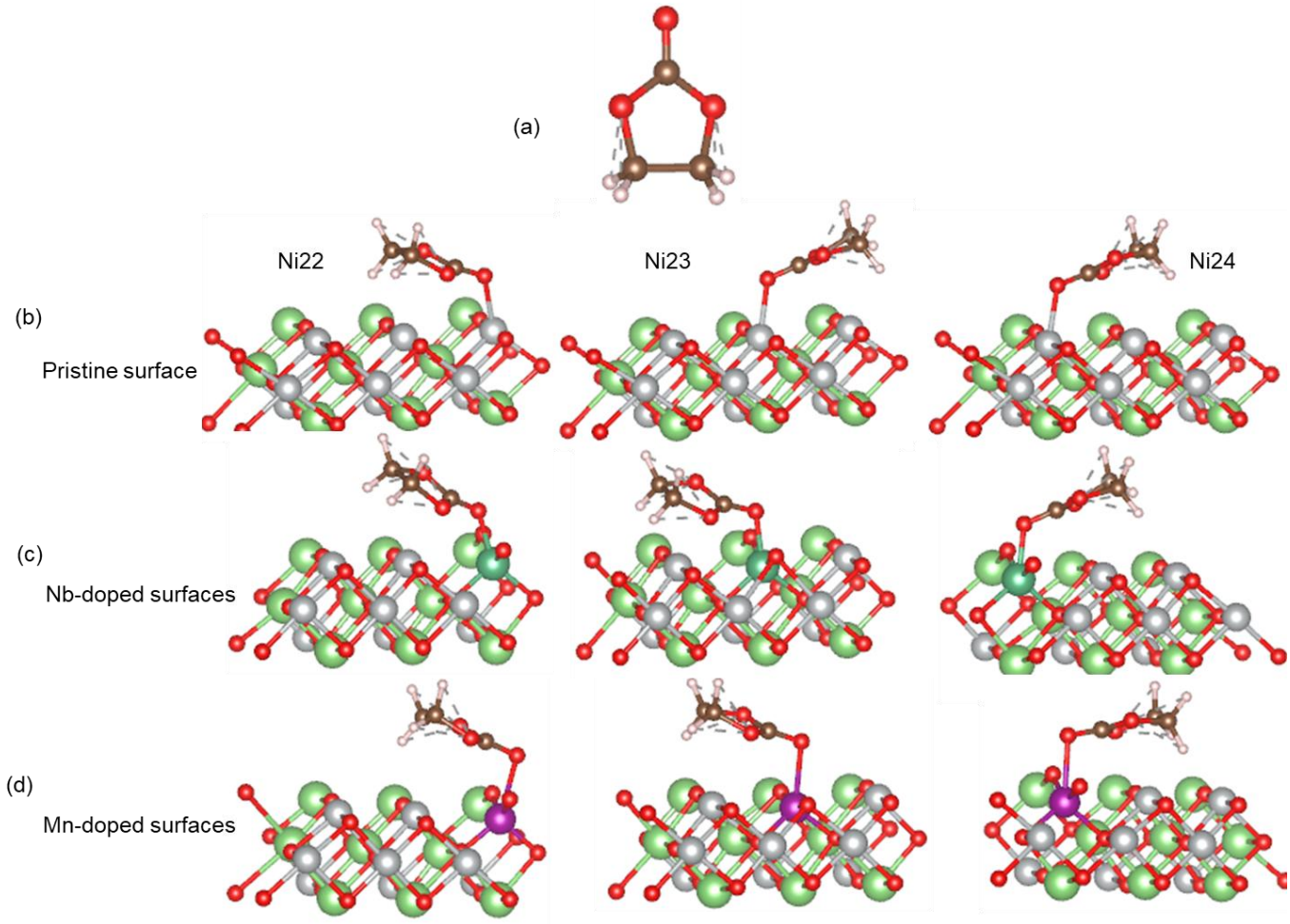

Figure 4.4: (a) EC molecule, (b) EC adsorbed on pristine sites, (c) EC adsorbed on Nb-doped, (d) EC adsorbed on Mn-doped on$LiNiO_2$ (101) surface on Ni site.

The EC molecule was initially positioned in our simulations at a distance of 1.907 Å, 1.921 Å, and 2.070 from the Nb, Mn, and Ni sites on the surface, respectively. The bond length was guided by the literature when Nb-O, Mn-O, and Ni-O were found to be 1.907 Å [202], 1.921 Å [203] and 2.070 Å [204] to enhance the attractive forces while minimizing the repulsive interactions between the component and the surface. During the geometry optimization, however, both the adsorbate and the surface were allowed to move freely and adjust their adsorption geometry. Table 4.4 below summarizes the interactions between the layered $LiNiO_2$ (101) surfaces and the EC molecule.

Table 4.4: Calculated adsorption energies of EC molecule on pristine and Nb/Mn-doped on $LiNiO_2$ (101) surface.

Surface Type	Doping Position	Adsorption Site	Adsorption Energy (eV)
Pristine	-	Ni_{22}	-1.100
	-	Ni_{23}	-1.120
	-	Ni_{24}	-0.976
Mn-doped	Ni_{22}	Ni_{22}	-1.316
	Ni_{23}	Ni_{23}	-1.990
	Ni_{24}	Ni_{24}	-1.089
Nb-doped	Ni_{22}	Ni_{22}	-2.677
	Ni_{23}	Ni_{23}	-3.127
	Ni_{24}	Ni_{24}	-2.909

The study investigates the adsorption of EC on the pristine and Nb/Mn-doped $LiNiO_2$ (101) surfaces, focusing on different nickel positions (Ni_{22}, Ni_{23}, and Ni_{24}). The adsorption energy of EC on the pristine $LiNiO_2$ (101) surface shows relatively weaker interactions across the different Ni positions. This suggests that the pristine surface has a lower affinity for EC molecules, which could be due to the less reactive nature of the surface's nickel sites in the absence of dopants. A comparison of EC adsorption energies on the doped and pristine surfaces reveals that doping notably increases the adsorption strength. Both Nb and Mn doping result in more negative adsorption energies, signifying stronger interactions between the EC molecule and the doped surfaces. This enhanced adsorption is particularly noticeable at specific nickel positions, suggesting that the presence of dopants increases the reactivity of these sites. The Nb doping shows the strongest adsorption energy, especially at the Ni_{23} position, where the adsorption energy reaches -3.027 eV. This is notably

stronger than the Mn-doped system, where the adsorption energies, while enhanced compared to the pristine surface, are still weaker than those observed with Nb doping. The stronger adsorption observed with Nb doping can be attributed to the larger atomic radius and higher valence electron count of Nb, which facilitates a more robust interaction with the EC molecule.

4.7 Summary

DFT simulations have been performed to study the effect of Nb/Mn doping and the adsorption of the EC molecule on the doped surface and pristine $LiNiO_2$ surface. The lithium-terminated (101) surface was found to be the most stable facet with the lowest surface energy of 0.117 eV/Å^2. Doping Nb/Mn on the Ni_{22} and Ni_{19} stabilizes the $LiNiO_2$ (101) surface on the top layer and second layer, respectively. The Nb-doped on the second layer has a lower surface free energy of 0.041 eV/Å^{2}than the Nb-doped on the top layer surface energy (0.057 eV/Å^2), but Mn-doped on the top layer has lower surface energy (0.093 eV/Å^2) compared to the surface energy (0.097 eV/Å^2) of Mn-doped on the second layer. However, the Nb-doped surface has a lower surface free energy of 0.041 eV/Å^2 compared to Mn-doped surface energy (0.093eV). This suggests that the Nb-doped $LiNiO_2$ (101) surface is more stable and has a reduced tendency to interact with its surroundings compared to the Mn-doped $LiNiO_2$ (101) surface. On the DOS the spin-up of the pristine surface has lower DOS around the Fermi level compared to the Nb/Mn-doped surface, which implies that is most stable. However, on the spin down we observe that Nb-doped (on second layer) surface has lowest DOS followed by Mn-doped (on top-layer). The DOS analysis in the spin-down channel aligns with the stability trend predicted by the surface free energy calculations. Doping on the second layers result in a lower ϕ = 5.190 eV and 5.23 eV for Mn and Nb, respectively. This implies that the surface with Mn-doped on

the second layer is more reactive than the Nb-doped surface on the second layer. The EC adsorbed on pristine and Mn/Nb-doped Ni_{23} (-1.120, -1.990, and -3.027) exhibits stronger adsorption compared to EC adsorption on Mn and Nb-doped Ni_{22} and Ni_{24}. This suggests that Mn and Nb doping on Ni_{23} creates more reactive sites for EC adsorption.

CHAPTER 5

5.1 CONCLUSION

DFT calculations were conducted to investigate the bulk properties, surface chemistry of stable low Miller index surfaces, the impact of Nb/Mn doping on the stable facets of $LiNiO_2$, and their interactions with the electrolyte component EC.

The calculated lattice parameters, volume, and heat of formation for monoclinic $LiNiO_2$ show excellent agreement with experimental data, confirming the reliability of the computational model. The lattice parameters (4.888 Å, 8.577 Å, and 4.928 Å) closely match experimental values (a=4.898 Å, b=8.450 Å, c=4.969 Å), with a minor volume deviation of just 7.31%. Additionally, the calculated heat of formation (−624.370 kJ/mol) aligns well with the experimental value (−619.00 kJ/mol), confirming the thermodynamic stability of the material. This stability is noteworthy, particularly in comparison to other materials like $LiCoO_2$ (heat of formation = −602 kJ/mol), positioning $LiNiO_2$ as a promising material for sustainable batteries.

To assess the mechanical stability of $LiNiO_2$, important for its application in lithium-ion batteries, we calculated the elastic constants. The results show that $LiNiO_2$ can withstand operational stresses, ensuring reliability and durability. The material satisfies the stability criteria for monoclinic materials, with high C_{11} (259.99 GPa) and C_{44} (60.87 GPa) values, indicating a strong structure. Pugh's ratio of 2.01 suggests that $LiNiO_2$ is ductile, which benefits battery performance, while the anisotropy factor (A=0.83) shows that the material's behavior under stress depends on the direction of the applied force, which may influence its deformation.

The electronic structure of $LiNiO_2$ reveals a half-metallic ferromagnetic nature, where the spin-up electrons are metallic, and the spin-down electrons behave like a semiconductor with a bandgap of 0.708 eV. This half-metallic behavior enhances electron movement in one direction while selectively controlling other charge carriers, improving the performance and energy efficiency of lithium-ion batteries. The PDOS analysis highlights the critical role of 3d-Ni and 2p-O orbitals near the Fermi level in shaping the material's electronic properties.

Phonon dispersion analysis suggests that the bulk structure of $LiNiO_2$ may experience some instability due to soft modes, primarily from oxygen vibrations. However, doping may help stabilize the material. Despite these potential instabilities, the overall thermodynamic and mechanical properties indicate that $LiNiO_2$ remains a stable and reliable material.

In our investigation of the seven low Miller index surfaces of $LiNiO_2$, the (101) surface was identified as the most stable and was chosen for further study. Surface energy calculations show that doping with Nb and Mn at the top and second layers reduces the surface free energy, enhancing stability. Among the two dopants, Nb doping in the second layer achieves the lowest surface energy (0.041 eV/Å²), followed by Mn doping in the top layer (0.093 eV/Å²), suggesting that both dopants help stabilize the surface. Electronic analysis shows that Nb doping transforms the material into a fully metallic state, improving its conductivity and overall stability. Nb-doped surfaces also exhibit a higher work function (5.232 eV for the first layer and 5.281 eV for the second layer) compared to Mn-doped surfaces, which reduces their chemical reactivity and enhances stability under operational conditions.

The adsorption of EC on both pristine and doped $LiNiO_2$ (101) surfaces shows that doping significantly enhances the adsorption process. The negative adsorption energies indicate that the adsorption is exothermic, suggesting favorable interactions between EC molecules and the surfaces. For the pristine $LiNiO_2$ (101) surface, the adsorption energies range from −1.100 eV at the Ni_{22} site to −1.120 eV at the Ni_{23} site, with the lowest adsorption energy of −0.976 eV at the Ni_{24} site. When Mn is introduced as a dopant, the adsorption energy increases, indicating stronger interaction with the EC molecule. On the Mn-doped $LiNiO_2$ (101) surface, the adsorption energy at the Ni_{23} site is the strongest at −1.990 eV, followed by −1.316 eV at the Ni_{22} site and −1.089 eV at the Ni_{24} site. For Nb doping, the adsorption energy further increases, with the lowest adsorption energy found at the Ni_{23} site (−3.127 eV), followed by −2.909 eV at the N_{i24} site and −2.677 eV at the Ni_{22} site.

This suggests that Nb doping significantly enhances the interaction with EC molecules compared to Mn doping and pristine surfaces. Among the doped surfaces, Nb doping in the top layer (Ni_{23}) results in the lowest adsorption energy, indicating the best interaction with EC. This improved compatibility with EC suggests that Nb-doped surfaces could contribute to better battery performance. While Mn doping also improves surface stability and EC adsorption, it does so to a lesser extent compared to Nb doping. Therefore, both Nb and Mn doping improve the stability and compatibility of the $LiNiO_2$ (101) surface with electrolyte components. However, Nb-doped surfaces demonstrate superior performance in terms of adsorption energy and interaction with EC, making Nb-doped $LiNiO_2$ (101) surfaces a promising candidate for high-performance lithium-ion batteries.

5.2 RECOMMENDATION

In light of the study findings, the following recommendations can be made regarding the stability and adsorption properties of $LiNiO_2$ surfaces for potential applications in energy storage systems:

The results indicate that the Nb-doped $LiNiO_2$ (101) surface exhibits the lowest surface free energy, suggesting superior stability over the pristine and Mn-doped surfaces. It is recommended that future studies and applications focus on Nb-doped $LiNiO_2$ surfaces, particularly for devices requiring stable cathode materials in lithium-ion batteries. The study reveals that EC adsorbs less effectively on pristine $LiNiO_2$ surfaces compared to doped ones, with the Nb-doped surface demonstrating the lowest adsorption energy. It is recommended to further investigate the interaction between EC and Nb-doped $LiNiO_2$ (101) surfaces to better understand how this adsorption behaviour influences battery performance.

5.3 FUTURE WORK

The future work will focus on the following aspects:

Bulk and Surface Fluorination: To perform the fluorination of both the bulk and surface of the layered $LiNiO_2$ cathode material using the cluster expansion method. Blending of $LiMn_2O_4$ and $LiNiO_2$ Surfaces: To explore the effects of blending $LiMn_2O_4$ and $LiNiO_2$ surfaces, focusing on their interface formation and interaction. Electrolyte Impact: To investigate the interaction of the electrolyte, particularly EC, with the pristine and fluorine-modified surfaces of $LiNiO_2$.

REFERENCES

[1] X. Han, J. Hua and M. Ouyang, "A review on the key issues for lithium-ion battery management in electric vehicles," *Journal of Power Sources,* vol. 226, p. 1, 2013.

[2] C. Liu, Z. Naele and G, cao, "Understanding electrochemical potentials of cathode materials in rechargeable batteries," *Materials Today,* vol. 19, no. 2, p. 1, 2016.

[3] Z. Chen, W, Zhang and Z. Yang, "A review on cathode materials for advanced lithium ion batteries: microstructure designs and performance regulations," *Nanotechnology,* vol. 31, p. 1, 2019.

[4] M. Li, J. Lu, Z. Chen and K. Amine, "30 Years of Lithium-Ion Batteries," *Advanced materials,* vol. 30, no. 1, pp. 1-2, 2018.

[5] A. Manthiram, "A reflection on lithium-ion battery cathode chemistry," *Nature communications,* vol. 11, pp. 1-2, 2020.

[6] N. Nitta, F. Wu, J. T. Lee and G.Yushin, "Li-ion battery materials: present and future," *Materials Today,* vol. 18, no. 5, p. 1, 2015.

[7] P.C. Jones, P.J. wiseman and J.B. Goodenough., "$L_{ix}CoO_2$ ($0<x\leqslant 1$): A new cathode material for batteries of high energy density," *Solid State Ionics,* Vols. 3-4, pp. 1-2, 1981.

[8] H.S. Ko, J.H. Kim, J. wang and J.D. Lee, "Co/Ti co-substituted layered $LiNiO_2$ prepared using a concentration gradient method as an effective cathode material for Li-ion batteries," *Journal of Power Sources,* vol. 372, p. 107, 2017.

[9] T. Toma, R. Maezono and K. Hongo, "Electrochemical Properties and Crystal Structure of Li+/H+ Cation Exchanged $LiNiO_2$," A*pplied Energy* Materials*.,* vol. 3, p. 4071, 2020.

[10] T. Ohzuku, A. Ueda and M. Nagayama, "Electrochemistry and Structural Chemistry of $LiNiO_2$ (R3m) for 4 Volt Secondary Lithium Cells," *The Electrochemical Society,* vol. 140, p. 4078, 1993.

[11] P. Kalyani and N. Kalaiselvi, "Various aspects of $LiNiO_2$ chemistry: A review," *Science and Technology of Advanced Materials,* vol. 6, pp. 689-703, 2005.

[12] X. Zhu, H. Chen, H. Zhan, D. Yang, and Y Zhou, "Synthesis and characterization of $LiNi_{0.85}Co_{0.15-2x}(TiMg)_xO_2$ as cathode materials for lithium-ion batteries," *Materials Chemistry and Physics,* vol. 88, no. 1, p. 145, 2004.

[13] S.H. Park, K.S. Park, Y.K. Sun, K.S. Nahm, and Y.S. Lee, "Structural and electrochemical characterization of lithium excess and Al-doped nickel oxides synthesized by the sol–gel method," *Electrochimica Acta,* vol. 46, no. 8, p. 1215, 2001.

[14] F. Wang, Z. Liu, X. Yuan, J. Mo, C. Li, L. Fu, Y. Zhu, X. Wu and Y. Wu, "A quasi-solid-state Li-ion capacitor with high energy density based on Li_3VO_4/carbon nanofibers and electrochemically-exfoliated graphene sheets," *Journal of Materials Chemistry,* vol. 5, pp. 14929-14992, 2017.

[15] J. Zheng, Y. Hou, Y. Duan, X. Song, Y. Wei, T. Liu, J. Hu, H. Guo, Z. Zhuo, L. Liu, Z. Chang, X. Wang, D. Zherebetskyy, Y. Fang, Y. Lin, K. Xu, L.W. Wang, Y. Wu and Pan, "Janus solid-liquid interface enabling ultrahigh charging and discharging rate for advanced lithium-ion batteries," *Nanoscoence Letters,* vol. 15, pp. 6102-6109, 2015.

[16] C.D. Sunesh, G. Mathai and Y. Choe, "Constructive effects of long alkyl chains on the electroluminescent properties of cationic iridium complex-based light-emitting electrochemical cells," *Advance Energy Materials,* vol. 8, p. Article 1701215, 2017.

[17] K. Shaju, G.S. Rao and B. Chowdari, "Performance of layered $Li(Ni_{1/3}Co_{1/3}Mn_{1/3})O_2$as cathode for Li-ion batteries," *Electrochemical Acta.,* vol. 48, no. 2, pp. 145-151, 2002.

[18] H.J. Kweon, S.J. Kim and D.G. Park, "An Ostwald ripening route towards Ni-rich layered cathode material with cobalt-rich surface for lithium-ion battery," *Journal Power sources,* vol. 88, p. 255, 2000.

[19] H. He, H. Cong, Y. Sun, L. Zan and Y. Zhang, "Spinel-layered integrate structured nanorods with both high capacity and superior high-rate capability as cathode material for lithium-ion batteries," *Nano Research,* vol. 10, pp. 55-56, 2017.

[20] R. Wang, X. He, L. He, F. Wang, R. Xiao, L. Gu, H. Li, and L. Chen, "Atomic structure of $L_{i2}MnO_3$ after partial delithiation and re-lithiation," *Advanced Energy Materials,* vol. 3, no. 10, pp. 1358-1367, 2013.

[21] Y. Gao, X. Wang, J. Ma, Z. Wang and L. Chen, "Selecting substituent elements for Li-rich Mn-based cathode materials by density functional theory (DFT) calculations," *Chemistry of Materials,* vol. 27, no. 9, pp. 3456-3461, 2015.

[22] P. Guan, L. Zhou, Z. Yu, Y. Sun, Y. Liu, F. Wu, Y. Jiang and D. Chu, "Recent progress of surface coating on cathode materials for high-performance lithium-ion batteries," *Journal of Energy Chemistry,* vol. 43, pp. 220-235, 2020.

[23] Z. Liu, X. Guo, N, Meng, Z, Yu and H. Yang, "Study of thermal runaway and the combustion behavior of lithium-ion batteries overcharged with high current rates," *Thermochimica Acta,* vol. 8, p. 3, 2022.

[24] X. Tang, S. Lv, K. Jiang, G. Zhou and Z. Liu, "Recent development of ionic liquid-based electrolytes in lithium-ion batteries," *Journal of Power Source,* vol. 542, pp. 1-2, 2022.

[25] I. Sourmey, "Application Engineer at Saft Connected Energy Division," *Energizing loT,* p. 1, 2022.

[26] S.M. Walake, "Study on Discharge characteristics of the Lithium - Ion battery," *International Journal of Innovative Research in Technology,* vol. 6, no. 11, p. 22, 2020.

[27] C. Yang, J. Chen, X. Ji, T.P. Pollard, X. Lü, C-J Sun, S. Hou, Q. Liu, C. Liu, T. Qing, Y.i Wang, O. Borodin, Y. Ren, K. Xu and C. Wang , "Aqueous Li-ion battery enabled by halogen conversion–intercalation chemistry in graphite," *nature ,* vol. 569, pp. 245-250, 2019.

[28] L. Ji, Z. Lin, M. Alcoutlabi and X. Zhang, "Recent developments in nanostructured anode materials for rechargeable lithium-ion batteries," *energy and enviromental science ,* vol. 8, p.

1, 2011.

[29] L. Li, H. Wang, Z. Xie, C. An. G. Jiang and Y. wang, “3D graphene-encapsulated nearly monodisperse Fe_3O_4 nanoparticles as high-performance lithium-ion battery anodes,” *Journal of Alloys and Compounds,* vol. 815, p. 1, 2020.

[30] C.K. Chan, H. Peng, G.Liu, K. McIlwrath, X.F. Zhang, R.A. Huggins and Y. Cui , “High-performance lithium battery anodes using silicon nanowires,” *nature nanotechnology ,* vol. 3, p. 31, 2007.

[31] E. Frackowiaka and F. Béguinb, “Electrochemical storage of energy in carbon nanotubes and nanostructured carbons,” *Carbon,* vol. 40, no. 10, p. 1776, 2002.

[32] C. Heubner, B. Mattheya, T. Lein, F. Wolke, T. Liebmann, C. Lämmel, M. Schneider and A. Michaelisa, “Insights into the electrochemical Li/Na-exchange in layered $LiCoO_2$ cathode material,” *Energy Storage Materials,* vol. 27, p. 377, 2020.

[33] M. A. Hannan, MD. Hoque, Y. Yusof and P.J. Ker, “State-of-the-art and energy management system of lithium-ion batteries in electric vehicle applications: issues and recommendations,” *IEEE Access,* vol. 6, p. 19364, 2018.

[34] R. Guo and W. Han , “The effects of electrolytes, electrolyte/electrode interphase, and binders on lithium-ion batteries at low temperature,” *Materials Today Sustainability,* p. 1, 2022.

[35] J. Garcia-Barriocanal, A. Rivera-Calzada, M. Arco, Z. Sefrioui and J. Santamaria, “Colossal ionic conductivity at interfaces of epitaxial ZrO_2:Y_2O_3/$SrTiO_3$ heterostructures,” *Science,* vol. 321, pp. 676-680, 2008.

[36] B. Kang and G. Ceder, “Battery materials for ultrafast charging and discharging,” *Nature,* vol. 458, pp. 190-193, 2009.

[37] L. Xia, C. Yu, Y. Fan, B. Li and Y. Xia, “Joint estimation of the state-of-energy and state-of-charge of lithium-ion batteries under a wide temperature range based on the fusion modeling and online parameter prediction,” *Journal of Energy storage,* vol. 52, p. 1, 2020.

[38] Z. Wei, “A noise-tolerant model parameterization method for lithium-ion battery management system,” *Applied Energy,* vol. 268, p. 114932, 2020.

[39] X.T. Liu, “An improved state of charge and state of power estimation method based on genetic particle filter for Lithium-ion batteries,” *Energies,* vol. 13, no. 2, 2020.

[40] K. Xu, “Nonaqueous liquid electrolytes for lithium-based rechargeable,” *Chemical Reviews,* vol. 104, pp. 4303-441, 2004.

[41] H. Niu, L. Wang, P. Guan, N. Zhang, C. Yan, M. Ding, X. Guo, T. Huang and X. Hu, “Recent Advances in Application of Ionic Liquids in Electrolyte of Lithium Ion Batteries,” *Journal of Energy Storage,* vol. 40, p. 2, 2021.

[42] Y. Ding, Z.P. Cano, A. Yu, J. Lu and Z. Chen, “Automotive li-ion batteries: current status and future perspectives,” *Electrochemical Energy Reviews,* vol. 2, pp. 1-28, 2019.

[43] H. Zhang, C. Li,G.G. Eshetu, S. Laruelle, S. Grugeon, K. Zaghib, C. Julien, A. Mauger and D.

Guyomard, “From Solid-Solution Electrodes and the Rocking-Chair Concept to Today’s batteries,” *Angewandtew Chemical International Edition,* vol. 59, pp. 534-538, 2020.

[44] L. Wang, Z. Hu, K. Zhao, Y. Luo, Q. Wei, C. Tang, P. Hu, W. Ren and L. Mai, “Hollow spherical $LiNi_{0.5}Mn_{1.5}O_4$ built from polyhedra with high-rate performance via carbon nanotube modification,” *Science China Materials,* vol. 59, pp. 95-103, 2016.

[45] J. Jung, C. Lee, S. Yu and I. Kim, “Electrospun nanofibers as a platform for advanced secondary batteries: a comprehensive review,” *Journal of materials Chemistry A,* vol. 4, pp. 703-750, 2016.

[46] F. Wang, X. Wu, X. Yuan, Z. Liu, Y. Zhang, L. Fu, Y. Zhu, Q. Zhou, Y. Wu and W. Huang, “Latest advances in supercapacitors: from new electrode materials to novel device designs,” *chemical society Reviews,* vol. 46, pp. 6816-6854, 2017.

[47] B.V.R. Chowdari, G.V.S. Rao and S.Y. Chow, “Cathodic behaviour of NiO-coated $Li(Ni_{1/2}Mn_{1/2})O_2$,” *Solid State Ionics,* vol. 140, p. 55, 2001.

[48] Y. Shi, M. Zhang, C. Fang and Y.S. Meng, “Urea-based hydrothermal synthesis of $LiNi_{0.5}Co_{0.2}Mn_{0.3}O_2$ cathode material for Li-ion battery,” *Journal of Power Source,* vol. 394, pp. 114-121, 2018.

[49] M. Bianchini, M. Roca-Ayats, P. Hartmann, T. Brezesinski and J. Janek, “There and Back Again—The Journey of $LiNiO_2$ as a Cathode Active material,” *Angewandtew Chemical International Edition,* vol. 58, no. 31, p. 10434, 2019.

[50] J. Wang, X. Qin, J. Gou, M. Zhou, B.O. Zong, L.I. Wang and G. Liang, “A porous hierarchical micro/nano $LiNi_{0.5}Mn_{1.5}O_4$ cathode material for Li-ion batteries synthesized by a urea-assisted hydrothermal method,” *Dalnton Trans.,* vol. 47, no. 21, pp. 7333-7343, 2018.

[51] J. Valikangas, P. Laine, M. Hietaniemi, T. Hu, P. Tynjala and U. Lassi, “Precipitation and calcination of high-capacity $LiNiO_2$ cathode material for lithium-ion batteries,” *Applied Science.,* vol. 10, pp. 1-11, 2020.

[52] S.N. Kwom, J. Song and D.R. Mumm, “Effects of cathode fabrication conditions and cycling on the electrochemical performance of $LiNiO_2$ synthesized by combustion and calcination,” *Ceram inernational.,* vol. 37, pp. 1543-1548, 2011.

[53] L.A. Montoro, M.A. Abbate, E.C. Almelda and J.M. Rosolen, “Electronic structure of the transition metal ions in $LiCoO_2$, $LiNiO_2$ and $LiCo_{0.5}Ni_{0.5}O_2$,” *Chemistry Physics Letter,* vol. 309, pp. 14-18, 1999.

[54] P. Cui, Z. Jiu. L. Li and T. He, “Preparation and characteristics of Sb-doped $LiNiO_2$ cathode materials for Li-ion batteries,” *Journal of Physics Chemistry Solid,* vol. 72, pp. 889-908, 2011.

[55] Q. Hao, F. Du, T. Xu, Q. Zhou, H. Cao, Z. Fan, C. Mei and J. Zheng, “Evaluation of Nb-Doping on performance of $LiNiO_2$ in wide temperature,” *Journal of Electroanalytical Chemistry,* vol. 907, p. 2, 2022.

[56] C. Kim, S.B. Yang, G.W. Yoo and J.T. Son,, “F-doped $0.5Li_2MnO_3 \cdot 0.5LiNi_{1/3}Co_{1/3}Mn_{1/3}O_2$ high porous nanofibers as cathode material for lithium-ion battery,” *Journal of Nanoscience and*

Nanotechnology, vol. 16, pp. 832-8346, 2016.

[57] B. Xu, D. Qian., Z. Wang and Y.S. Meng, "Recent progress in cathode materials research for advanced lithium ion batteries," *Materials Science and Engineering,* vol. 73, pp. 54-65, 2012.

[58] B. Scrosati, "Recent advances in lithium ion battery materials," *Electrochimica Acta,* vol. 45, pp. 2461-2466, 2000.

[59] C. Liu, Z.G. Neale. and G. Cao, "Understanding electrochemical potentials of cathode materials in rechargeable batteries," *Materials Today,* vol. 22, p. 109, 2016.

[60] D. Djian, F. Alloin, S. Martinet, H. Lignier and J.Y. Sanchez, "Lithium-ion batteries with high charge rate capacity: Influence of the porous separator," *Journal of Power Sources,* vol. 172, pp. 416-421, 2007.

[61] J.M. Tarascon and D. Guyomard, "Li metal-free rechargeable batteries based on $Li_{1+x}Mn_2O_4$ cathodes ($0 \leq x \leq 1$) and carbon anodes," *Journal of The Electrochemical Society,* vol. 138, pp. 2864-2868, 1991.

[62] Y. Xia, H. Takeshige, H. Noguchi and M. Yoshio, "Studies on an Li-Mn-O spinel system (obtained by melt-impregnation) as a cathode for 4V lithium batteries part 1. Synthesis and electrochemical behaviour of $Li_xMn_2O_4$," *Journal of Power Sources,* vol. 56, p. 6167, 1995.

[63] Q. Lu, J.G. Chen and J.Q Xiao, "Nanostructured electrodes for high-performance pseudocapacitors," *Angewandte Chemie International Edition,* vol. 52, pp. 1882-1889, 2013.

[64] M.S. Islam and C.A. Fisher, "Lithium and sodium battery cathode materials: computational insights into voltage, diffusion and nanostructural properties.," *Chemical Society Reviews,* vol. 43, pp. 185-204, 2014.

[65] E. Shinova, E.hecheva, R. Stoyanova and G.D. Bromiley, "High-pressure synthesis of solid solutions between trigonal $LiNiO_2$ and monoclinic $Li[Li_{1/3}Ni_{2/3}]O_2$," *Journal of Solid State Chemistry,* vol. 178, no. 5, p. 1664, 2005.

[66] J.Cao, H. Zou, C. Guo, Z. Chen and S. Pu, "Local trimer orbital ordering in $LiNiO_2$ studied by quantitative convergent beam electron diffraction technique," *Solid State Ionics,* vol. 180, 2009.

[67] K. Chang, B. Hallstedt and D. Music, "Thermodynamic and Electrochemical Properties of the Li−Co−O and Li-Ni-O system," *Chemestry of Materials,* vol. 37, pp. 100-107, 2012.

[68] M. Tuccillo, O. Palumbo, M. Pavone, A.B. Muñoz-García, A. Paolone and S. Brutti, "Analysis of the Phase Stability of $LiMO_2$ Layered Oxides (M = Co, Mn, Ni)," *Crystals,* vol. 10, no. 526, p. 10, 2020.

[69] T.A. Taha and M.M El-Molla, "Green simple preparation of $LiNiO_2$ nanopowder for lithium ion battery," *jounal of Materials Research and Technology,* vol. 9, no. 4, p. 7955, 2020.

[70] K. Mizushima, P.C. Jones, P.J. Wiseman, and J.B. Goodenough, "Li_xCoO_2 ($0 < x \leq 1$): A new cathode material for batteries of high energy density," *Solid State Ionic,* vol. 3, pp. 171-174, 1981.

[71] T.T.B. Tran, E-J. Park, H-I. Kim, S-H. Lee, H-J. Jang and J-T. Son, "High rate performance of Lithium-ion batteries with Co-free $LiNiO_2$ cathode," *Materials Letters ,* vol. 316, p. 1, 2022.

[72] T. Rao, P. Gao, Z. Zhu, S. Wang, L. Ben and Y. Zhu, "Structural, electrochemical, and Li-ion diffusion properties of Mg&Mn dual doped $LiNiO_2$ cathode materials for Li-ion batteries," *Solid State Ionics,* vol. 376, p. 1, 2022.

[73] H-W. Ha, K.H. Jeong and K. Kim, "Effect of titanium substitution in layered $LiNiO_2$ cathode material prepared by molten-salt synthesis," *Journal of Power Sources,* vol. 161, p. 606, 2006.

[74] T. Ohzuku and A. Ueda, "Why transition metal (di) oxides are the most attractive materials for batteries," *Solid State Ionics,* vol. 69, no. 3-4, pp. 201-211, 1994.

[75] M. Broussely, F. Perton, P. Biensan, J.M. Bodet, J. Labat, A. Lecerf, C. Delmas, A. Rougier and J.P. Pérès, "Li_xNiO_2, a promising cathode for rechargeable lithium batteries," *Journal of Power Sources,* vol. 54, no. 1, pp. 109-114, 1995.

[76] L. Lu, X. Han, J. Li, J. Hua and M. Ouyang, "A review on the key issues for lithium-ion battery management in electric vehicles," *Journal of Power Sources,* vol. 226, pp. 272-288, 2013.

[77] W.B. Luo, L. Wen, H.Z Luo, R.S. Song, Y.C. Zhai, C. Liu, and F. Li, "Carbon nanotube-modified $LiFePO_4$ for high rate lithium ion batteries," *New Carbon Materials,* vol. 29, pp. 287-294, 2014.

[78] S.-H. Kang and M. Thackeray, " Stabilization of $xLi_2MnO_3 \cdot (1- x)$ $LiMO_2$ Electrode Surfaces (M= Mn, Ni, Co) with Mildly Acidic, Fluorinated Solutions," *Journal of the Electrochemical Society,* vol. 155, pp. A269-A275, 2008.

[79] X. Wang, S. Dong, and H. Wang, "Design and fabrication of N-doped graphene decorated LiFePO4@ C composite as a potential cathode for electrochemical energy storage," *Ceramics International,* vol. 44, no. 1, pp. 464-470, 2018.

[80] H.-J. Noh, S. Youn, C.S. Yoon and Y.-K. Sun, "Comparison of the structural and electrochemical properties of layered Li $[Ni_xCo_yMn_z]O_2$ (x= 1/3, 0.5, 0.6, 0.7, 0.8 and 0.85) cathode material for lithium-ion batteries," *Journal of Power Sources ,* vol. 233, pp. 121-130, 2013.

[81] Z.-L. Chen, Y.-J. Gu, Y.-L. Huo, X.-Y. Ma and F.-Z. Wu, "Enhanced electrochemical performance of manganese-based metal organic frameworks-derived spinel $LiMn_2O_4$ cathode materials by improving the Mn^{3+} content and oxygen vacancies," *Journal of Alloys and Compounds,* vol. 917, p. 2, 2022.

[82] D. Guo, X. Wei, Z. Chang, H. Tang, B. Li, E. Shangguan, K. Chang, X.-Z. Yuan and H. Wang, "Synthesis and electrochemical properties of high performance polyhedron sphere like lithium manganese oxide for lithium ion batteries," *Journal of Alloys and Compounds,* vol. 632, pp. 222-228, 2015.

[83] M. Rao, "$LiMn_2O_4$ Cathodes for solid state lithium-ion batteries-energy storage and conversion," *Journal of Optoelectron. Biomed. Mater,* vol. 5, no. 1, pp. 9-16, 2013.

[84] X. Xiao, J. Lu and Y. Li, "$LiMn_2O_4$ microspheres: Synthesis, characterization and use as a cathode in lithium ion batteries," *Nano Res.,* vol. 3, pp. 733-737, 2010.

[85] S.-T. Myung, K. Amine and Y.-K. Sun, “Nanostructured cathode materials for rechargeable lithium batteries,” *Journal of Power Sources,* vol. 283, pp. 219-236, 2015.

[86] Z. Kai, W. Yang, Z. Shuang, Y. Yan, P. Hao, L. Guiwei and J. Jianli, “Synthesis of single crystalline spinel $LiMn_2O_4$ nanorods for a lithium ion battery,” *International Journal of Electrochemestry. Science.,* vol. 9, no. 9, pp. 5280-5288, 2014.

[87] B. Ebin, V. Battaglia and S. Gürmen, “Comparison of 4 V and 3 V electrochemical properties of nanocrystalline $LiMn_2O_4$ cathode particles in lithium ion batteries prepared by ultrasonic spray pyrolysis,” *Ceramics International,* vol. 40, no. 5, pp. 7029-7035, 2014.

[88] H.-W. Ha, N.J. Yun and K. Kim, “Improvement of electrochemical stability of $LiMn_2O_4$ by CeO_2 coating for lithium-ion batteries,” *Electrochim. Acta, ,* vol. 52, pp. 3236-3241, 2007.

[89] D. Zhang, B.N. Popov and R.E. White, “Electrochemical investigation of $CrO_{2.65}$ doped $LiMn_2O_4$ as a cathode material for lithium-ion batteries,” *Journal of Power Source,* vol. 76, pp. 81-90, 1998.

[90] S. Kuwabata, S. Masui and H. Yoneyama, “Charge-discharge properties of composites of $LiMn_2O_4$ and polypyrrole as positive electrode materials for 4 V class of rechargeable Li batteries,” *Electrochim. Acta,* vol. 44, pp. 4593-4600, 1999.

[91] Y. Lin, M.X. Gao, D. Zhu, Y.F. Liu and H.G. Pan, “Effects of carbon coating and iron phosphides on the electrochemical properties of $LiFePO_4$/C,” *Journal Power Source,* vol. 184, pp. 444-448, 2008.

[92] J. He, Y. Zhang, Y. Zhang, P. Dong, H. Shi, Y. Li, Z. Liang, Y. Xiang. J. Dang. and D. wang, “Layered over-lithiated oxide coating for reviving spent $LiCoO_2$ cathode for stable high-voltage lithium-ion battery,” *Journal of Alloys and Compounds,* vol. 908, p. 1, 2022.

[93] J.B. Goodenough, “Evolution of strategies for modern rechargeable batteries,” *Acc. Chem. Res., ,* vol. 46, pp. 1053-1061, 2013.

[94] M.S. Whittingham, “Lithium batteries and cathode materials,” *Chem. Rev.,* vol. 104, pp. 4271-4302, 2004.

[95] Q. Liu, X. Su, D. Lei, Y. Qin, J. Wen, F. Guo, Y.A. Wu, Y. Rong, R. Kou, X. Xiao, F. Aguesse, J. Bareño, Y. Ren, W. Lu and Y. Li, “Approaching the capacity limit of lithium cobalt oxide in lithium ion batteries via lanthanum and aluminium doping,” *Nat. Energy,* vol. 3, pp. 936-943, 2018.

[96] K. Wang, J. Wan, Y. Xiang, J. Zhu, Q. Leng, M. Wang, L. Xu and Y. Yang, “Recent advances and historical developments of high voltage lithium cobalt oxide materials for rechargeable Li-ion batteries,” *Journal of Power Sources,* vol. 460, p. 1, 2020.

[97] C. Wang, J. Weng, S. Wu, X. Zhang, Q. Tong and M. Zhu, “A review - exploring the performance degradation mechanisms of $LiCoO_2$ cathodes at high voltage conditions and some optimizing strategies,” *Mater. Chem. Front.,* vol. 6, pp. 2319-2337, 2022.

[98] K.X. Wang, X.H. Li and J.S. Chen, “Surface and interface engineering of electrode materials for

lithium-ion batteries," *Adv. Mater.,* vol. 27, pp. 527-545, 2015.

[99] Z. Chen and J.R. Dahn, "Studies of $LiCoO_2$ coated with metal oxides," *Electrochem. Solid State Lett.,* vol. 6, p. 1, 2003.

[100] Y. Iriyama, H. Kurita, I. Yamada, T. Abe and Z. Ogumi, "Effects of surface modification by MgO on interfacial reactions of lithium cobalt oxide thin film electrode," *J. Power Sources,* vol. 137, pp. 111-116, 2004.

[101] S.S. Jayasree, S. Nair and D. Santhanagopalan, "Ultrathin TiO_2 coating on $LiCoO_2$ for improved electrochemical performance as Li–ion battery cathode," *Chemistry Select, ,* vol. 3, pp. 2763-2766, 2018.

[102] Y. Oh, D. Ahn, S. Nam and B. Park, "The effect of Al_2O_3-coating coverage on the electrochemical properties in $LiCoO_2$ thin films," *Journal of Solid State Electrochem.,* vol. 14, pp. 1235-1240, 2010.

[103] Y. Orikasa, "Origin of surface coating effect for MgO on $LiCoO_2$ to improve the interfacial reaction between electrode and electrolyte," Advanced Materials Interfaces*,* vol. 1, pp. 1-8, 2014.

[104] S. Jantrasee, P. Moontragoon and S. Pinitsoontorn, "Thermoelectric properties of Al-doped ZnO: experiment and simulation," *Journal of Semiconductors,* vol. 37, pp. 1-7, 2016.

[105] A.J. Ghazai, E.A. Salman and Z.A. Jabbar, "Effect of aluminum doping on zinc oxide thin film properties synthesis by spin coating method," *American Scientific Research Journal for Engineering, Technology, and Sciences,* vol. 26, pp. 202-211, 2016.

[106] J. Kim, H. Lee, H. Cha, M. Yoon, M. Park and J. Cho, "Prospect and reality of Ni-rich cathode for commercialization," *Advance Energy Materials,* vol. 8, p. 1702028, 2018.

[107] J. Liu, J. Wang, Y. Ni, K. Zhang, F. Cheng, J. Chen, "Recent breakthroughs and perspectives of high-energy layered oxide cathode materials for lithium ion batteries," *Materials Today,* vol. 43, pp. 132-165, 2021.

[108] J.B. Goodenough, "How we made the Li-ion rechargeable battery," *Nat. Electron.,* vol. 1, p. 204, 2018.

[109] J. Qian, L. Liu, J. Yang, S. Li, X. Wang, H. Zhuang and Y. Lu, "Electrochemical surface passivation of $LiCoO_2$ particles at ultrahigh voltage and its applications in lithium-based batteries," *Nat. Commun.,* vol. 9, p. 4918, 2018.

[110] H. Yu, Y. Qian, M.R. Otani, D. Tang, S. Guo, Y. Zhu and H. Zhou, "Study of the lithium/nickel ions exchange in the layered $LiNi_{0.42}Mn_{0.42}Co_{0.16}O_2$ cathode material for lithium ion batteries: experimental and first-principles calculations," *Energy Enviromenal Science,* vol. 7, pp. 1068-1078, 2014.

[111] M. Jiang, D.L. Danilov, R.A. Eichel, and P.H.L. Notten, "A Review of degradation mechanisms and recent achievements for Ni-rich cathode-based Li-ion batteries," *Advance Energy Materials,* vol. 11, p. 2103005, 2021.

[112] J.-H. Ju and K.-S. Ryu, “Synthesis and electrochemical performance of $Li(Ni_{0.8}Co_{0.15}Al0_{.05})0.8(Ni_{0.5}Mn_{0.5})_{0.2}O_2$ with core–shell structure as cathode material for Li-ion batteries,” *Journal of Alloys Compound,* vol. 509, pp. 7985-7992, 2011.

[113] Z. Liu, Z. Wang, T. Lu, P. Dai, P. Gao and Y. Zhu, “Modification of $LiNi_{0.8}Co_{0.15}Al_{0.05}O_2$ using nanoscale carbon coating,” *Journal of Alloys Compound ,* vol. 763, pp. 701-710, 2019.

[114] Y. Chen, Y. Lu, Z. Liu, L. Zhou, Z. Li, J. Jiang, L. Wei, P. Ren and T. Mu, “Efficient dissolution of lithium-ion batteries cathode $LiCoO_2$ by polyethylene glycol-based deep eutectic solvents at mild temperature,” *ACS Sustainable Chemistry & Engineering ,* vol. 8, pp. 11713-11720, 2020.

[115] J.R. Croy, B.R. Long and M. Balasubramanian, “A path toward cobalt-free lithium-ion cathodes,” *J. Power Sources,* vol. 440, pp. 1-2, 2019.

[116] R. Guo, Y. He, T. Yu, P. Cheng, J. You, H. Lin, C. Chen, T. Chan, X. Liu and Z. Hum, “Enhanced oxygen evolution reaction activity of flower-like FeOOH via the synergistic effect of sulfur,” *Chemical Engineering Journals,* vol. 420, pp. 1-2, 2021.

[117] T. Deng, X. Fang, L. Cao, J. Chen, S. Hou, X. Ji, L. Chen, S. Li, X. Zhou and E. Hu, “Designing in-situ-formed interphases enables highly reversible cobalt-free $LiNiO_2$ cathode for Li-ion and Li-metal batteries,” *Joule,* vol. 3, pp. 2550-2564, 2019.

[118] Y. Kobayashi, M. Tabuchi, H. Miyashiro and N. Kuriyama, “A new design of highly reversible $LiNiO_2$: defect formation in transition metal site,” *Journal of Power Sources,* vol. 364, pp. 156-162, 2017.

[119] J.B. Goodenough and Y. Kim, “Challenges for rechargeable Li batteries,” *Chemistry Materials,* vol. 22, pp. 587-603, 2010.

[120] H. Kim, A. Choi, S.W. Doo, J. Lim, Y. Kim and K.T. Lee, “Role of Na^+ in the cation disorder of $[Li_{1-x}Na_x]NiO_2$ as ac athode for lithium-ion batteries,” *Journal of Electrochemical Society,* vol. 165, pp. A201-A205, 2018.

[121] S. Zhang, P. Gao, Y. Wang, J. Li and Y. Zhu, “Cobalt-free concentration-gradient $Li[Ni_{0.9}Mn_{0.1}]O_2$ cathode material for lithium-ion batteries,” *Journal of Alloys Compound,* vol. 885, p. Article 161005, 2021.

[122] Y. Wang and Y. Zhu, “P. Gao. Synthesis and characterization of Nickel-rich layered $LiNi_{1-x}Mn_xO_2$ (x=0.02,0.05) cathodes for lithium-ion batteries,” *Electrochemical. Acta,,* vol. 427, p. Article 140891, 2022.

[123] H.-H. Ryu, G.-T. Park, C.S. Yoon and Y.-K. Sun, “Suppressing detrimental phase transitions via tungsten doping of $LiNiO_2$ cathode for next-generation lithium-ion batteries,” Journal of Materials Chemistry A*.,* vol. 7, pp. 18580-18588, 2019.

[124] C. Pouillerie, L. Croguennec and C. Delmas, “The $L_{ix}Ni_{1-y}Mg_yO_2$ (y=0.05, 0.10) system: structural modifications observed upon cycling,” *Solid State Ion,* vol. 132, pp. 15-29, 2000.

[125] C.S. Yoon, M.J. Choi, D.W. Jun, Q. Zhang, P. Kaghazchi, K.H. Kim and Y.K. Sun, “Cation ordering of Zr-doped $LiNiO_2$ cathode for lithium-ion batteries,” *Chemical Materials,* vol. 30, pp. 1808-

1814, 2018.

[126] J. Cho, T.-J. Kim, Y.J. Kim and B. Park, "High-performance ZrO_2-coated $LiNiO_2$ cathode material, Electrochem," *Solid-State Lett.,* vol. 4, pp. A159-A161, 2001.

[127] P. Mohan and G.P. Kalaignan, "Electrochemical performance of La_2O_3-coated layered $LiNiO_2$ cathode materials for rechargeable lithium-ion batteries," *Ionics,* vol. 19, pp. 895-902, 2013.

[128] N. Zhang, N. Zaker, H. Li, A. Liu, J. Inglis, L. Jing, J. Li, Y. Li, G.A. Botton and J.R. Dahn, "Cobalt-free nickel-rich positive electrode materials with a core-shell structure," *Chemical of Materials,* vol. 31, pp. 10150-10160, 2019.

[129] S. Karimzadeh, B. Safaei, W. Huang and T-C Jen, "Theoretical investigation on niobium doped $LiFePO_4$ cathode material for high performance lithium-ion batteries," *Journal of Energy Storage,* vol. 67, p. 1, 2023.

[130] M.A. Pellow, H. Ambrose, D. Mulvaney, R. Betita and S. Shaw,, "Research gaps in environmental life cycle assessments of lithium ion batteries for grid-scale stationary energy storage systems: end-of-life options and other issues," *Sustainable* Materials and *Technologies,* vol. 23, p. e00120, 2020.

[131] P. Greim, A.A. Solomon and C. Breye, "Assessment of lithium criticality in the global energy transition and addressing policy gaps in transportation," *Nature communications,* vol. 11, pp. 1-11, 2020.

[132] G. Chaudhary, J.J. Lamb, O.S. Burheim and B. Austbø, "Review of energy storage and energy management system control strategies in microgrids," *Energies,* vol. 14, p. 4929, 2021.

[133] W. Ebner, D. Fouchard and L. Xie, "The LiNiO2/carbon lithium-ion battery," *Journal of Power Sources,* vol. 68, p. 238, 1994.

[134] J.M. Tarascon, E. Wang, F.K. Shokoohi, W.R. Mekinnon and S. Colsons, "The Spinel Phase of $LiMn_2O_4$ as a Cathode in Secondary Lithium Cells," *Journal of The Electrochemical Society,* vol. 138 , p. 2859, 1991.

[135] L. Wang, Y.G. Sun, L.L. Hu, J.Y. Piao, J. Guo, A. Manthiram, J.M. Ma and A.M. Cao, "Copper-substituted $Na_{0.67}Ni_{0.3-x}Cu_xMn_{0.7}O_2$ cathode materials for sodium-ion batteries with suppressed P2-O2 phase transition," *J. Mater. Chem,* vol. 5, pp. 8752-8761, 2017.

[136] G.Y. Li, Z.J. Zhang, R.N. Wang, Z.L. Huang, Z.C. Zuo and H.H. Zhou, "Effect of trace Al surface doping on the structure, surface chemistry and low temperature performance of $LiNi_{0.5}Co_{0.2}Mn_{0.3}O_2$ cathode," *ectrochemical Acta,* vol. 212, pp. 399-407, 2016.

[137] Q.N. Sa, J.A. Heelan, Y. Lu, D. Apelian and Y. Wang, "Copper impurity effects on $LiNi_{1/3}Mn_{1/3}Co_{1/3}O_2$ cathode material," *ACS Applied Materials,* vol. 7, pp. 20585-2059, 2015.

[138] A. Milewska, M. Molenda and J. Molenda, "Structural, transport and electrochemical properties of $LiNi_{1-y}Co_yMn_{0.1}O_2$ and Al, Mg and Cu-substituted $LiNi_{0.65}Co_{0.25}Mn_{0.1}O_2$ oxides," *Solid State Ionics,* vol. 192, pp. 313-320, 2011.

[139] Y. Zhang, Z.B. Wang, F.D. Yu, L.F. Que, M.J. Wang, Y.F. Xia, Y. Xue and J. Wu, "Studies on

stability and capacity for long-life cycle performance of $Li(Ni_{0.5}Co_{0.2}Mn_{0.3})O^{-2}$ by Mo modification for lithium-ion battery," *Journal of Power Sources,* vol. 385, pp. 1-12, 2017.

[140] X.L. Yuan, Q.J. Xu, X.N. Liu, W. Shen, H.M. Liu and Y.Y. Xia, "Excellent rate performance and high capacity of Mo doped layered cathode material Li $Li_{0.2}Mn_{0.54}Ni_{0.13}Co_{0.13}O^{-2}$ derived from an improved coprecipitation approach," *Electrochimica Acta,* vol. 207, pp. 120-129, 2016.

[141] X. Feng, Y.R. Gao, L.B. Ben, Z.Z. Yang, Z.X. Wang and L.Q. Chen, "Enhanced electrochemical performance of Ti-doped $Li_{1.2}Mn_{0.54}Co_{0.13}Ni_{0.13}O_2$ for lithium-ion batteries," *Journal of Power Sources ,* vol. 317, pp. 74-80, 2016.

[142] S.U. Woo, B.C. Park, C.S. Yoon, S.T. Myung, J. Prakash and Y.K. Sun, "Improvement of electrochemical performances of $LiNi_{0.8}Co_{0.1}Mn_{0.1}O_2$ cathode materials by fluorine substitution," *Journal of Electrochemical Society,* vol. 154, pp. A649-A655, 2007.

[143] C. Kim, S.B. Yang, G.W. Yoo and J.T. Son, "F-doped $0.5Li_2MnO_3 \cdot 0.5\ LiNi_{1/3}Co_{1/3}Mn_{1/3}O_2$ high porous nanofibers as cathode material for lithium-ion battery," *Journal of Nanoscience and Nanotechnology,* vol. 16, no. 8, pp. 8342-8346, 2016.

[144] L. Li, B.H. Song, Y.L. Chang, H. Xia, J.R. Yang, K.S. Lee and L. Lu, "Retarded phase transition by fluorine doping in Li-rich layered $Li_{1.2}Mn_{0.54}Ni_{0.13}Co_{0.13}O_2$ cathode material," *Journal of Power Sources,* vol. 283, p. 162e170, 2015.

[145] H. Kim, D. Byun, W. Chang, H.-G. Jung and W. Choi, "A nano-$LiNbO_3$ coating layer and diffusion-induced surface control towards high-performance 5 V spinel cathodes for rechargeable batteries," *Journal of Materials Chemistry,* vol. 5, pp. 25077-25089, 2017.

[146] W. Li, E.M. Erickson and A. Manthiram, "High-nickel layered oxide cathodes for lithium-based automotive batteries," *Nat. Energy,* vol. 5, pp. 26-34, 2020.

[147] D. Aurbach, B. Markovsky, Y. Talyossef, G. Salitra, H.-J. Kim and S. Choi, "Studies of cycling behavior, ageing, and interfacial reactions of $LiNi_{0.5}Mn_{1.5}O_4$ and carbon electrodes for lithium-ion 5-V cells," *Journal of Power Sources,* vol. 162, p. 780, 2006.

[148] S. Shi, J. Gao, Y. Liu, Y. Zhao, Q. Wu, W. Ju, C. Ouyang and R. Xiao, ""'Multiscale computation methods: their applications in lithium-ion battery research and development," *Chinese Physics B,* vol. 25, p. 18212, 2015.

[149] M.D. Segall, P.J.D. Lindan, M.J. Probert, C.J. Pickard, P.J. Hasnip, S.J. Clark and M.C. Payne, "First principle simulations: Ideas, illustrations and the CASTEP code," *Physical Review B,* vol. 14, pp. 2717-2744, 2002.

[150] R.G. Vignale, "DFT in magnetic fields," *Physical Review Letters,* vol. 59, pp. 2360-2363, 1979.

[151] J.E. Moyal, "Quantum mechanics as a statistical theory," *Mathematical Proceedings of the Cambridge Philosophical Society,* vol. 12, pp. 190-196, 1949.

[152] P. Hohenberg and W. Kohn, "Inhomogeneous electron gas," *Physical Review,* vol. 136, pp. B864-B864, 1964.

[153] C.C.M. Rindt and S.V. Gaastra-Nedea, "Modeling thermochemical reactions in thermal energy

storage systems," *In Advances in Thermal Energy Storage Systems,* vol. 4, pp. 375-375, 2015.

[154] A.D. Blecke, "A new mixing of Hartree–Fock and local density-functional theories," *The Journal of Chemical Physics,* vol. 98, pp. 1372-1377, 1993.

[155] A.E. Mattsson, P.A. Schultz, M.P. Desjarlais, T.R. Mattsson and K. Leung, "Designing meaningful density functional theory calculations in material science," *Modelling and Simulation in Materials Science and Engineering,* vol. 13, p. 31, 2005.

[156] K. Horn and M. Scheffler, in *Electronic structure*, vol. 2, Amsterdam, The Netherlands: Elsevier, 2000.

[157] D.J.W. Geldart and M. Rasolt, "Exchange and correlation energy of an inhomogeneous electron gas at metallic densities," *Physical Review B,* vol. 13, no. 4, p. 1477, 1976.

[158] P.A. Dirac, "Note on exchange phenomena in the Thomas atom," *in Mathematical Proceedings of the Cambridge Philosophical Society, Cambridge, Cambridge University Press,* pp. 376-385, 1930.

[159] R.G. Parr, "Density-Functional Theory of Atoms and Molecules," in *Horizons of Quantum chemistry*, springer, 1980, pp. 5-15.

[160] E, Engel and J.P. Perdew, "Theory of metallic clusters: Asymptotic size dependence of electronic properties," *Physical Review B,* vol. 43, no. 2, pp. 1-7, 1991.

[161] G. Kresse and D. Joubert,, "From ultrasoft pseudopotentials to the projector augmented-wave method," *Physical Review B,* vol. 19, no. 3, pp. 1758-1775, 1999.

[162] A. St.-Amant, W.D. Cornell, P.A. Kollman and T.A. Halgren, "Calculation of molecular geometries, relative conformational energies, dipole moments, and molecular electrostatic potential fitted charges of small organic molecules of biochemical interest by density functional theory," *Journal of computational chemistry,* vol. 16, no. 12, pp. 1483-1506, 1995.

[163] P. Politzer and J.M. Seminario, "Modern density functional theory," in *a tool for chemistry*, LausanneNew York- Oxford- Shannon- Tokyo, Elsevier, 1995.

[164] A.D. Becke, "Density-functional exchange-energy approximation with correct asymptotic behavior," *Physical review A,* vol. 36, no. 6, p. 3098, 1988.

[165] J.P. Perdew, "Density-functional approximation for the correlation energy of the inhomogeneous electron gas," *Physical Review B,* vol. 33, no. 12, p. 8822, 1986.

[166] J.P. Perdew and Y. Wang, "Accurate and simple density functional for the electronic exchange energy: Generalized gradient approximation," *Physical review B ,* vol. 33, no. 12, p. 8800, 1986.

[167] P Ziesche, J.P. Perdew and H. Eschrig, "Electronic structure of solids' 91," Berlin, Akademie Verlag, 1991.

[168] M.C. Payne, M.P. Teter, D.C. Allan, T.A. Arias and A.J. Joannopoulo, "Iterative minimization techniques for ab initio total-energy calculations: molecular dynamics and conjugate gradient," *Reviews of modern physics,* vol. 64, no. 4, pp. 1045-1097, 1992.

[169] J.P. Perdew, K. Burke and Y. Wang, “Generalized gradient approximation for the exchangecorrelation hole of a many-electron system,” *Physical Review B,* vol. 54, no. 23, pp. 16533-16539, 1996.

[170] J.C. Phillips and L. Kleinman, “New method for calculating wave functions in crystals and molecules,” *Physical Review,* vol. 116, no. 2, p. 287, 1959.

[171] V. Heine and D. Weaire, “Pseudopotential theory of cohesion and structure,” *Solid state physics,* vol. 24, pp. 249-263, 1970.

[172] P.E. Blöchl, “Projector augmented-wave method,” *Physical review B,* vol. 50, no. 24, pp. 17953-17979, 1994.

[173] T. Cottenier, A. Van Den Berg and T. Elrad, “Modeling aspect-oriented compositions,” in *in International Conference on Model Driven Engineering Languages and Systems*, Berlin, Heidelberg, Springe, 2005, pp. 100-109.

[174] G. Kresse, M. Marsman and J. Furthmüller, “VASP the GUIDE, Computational Physics,” *Faculty of Physics, Universität Wien Sensengasse,* vol. 8, 2009.

[175] D. Vanderbilt , “Soft self-consistent pseudopotentials in a generalized eigenvalue formalism,” *Physical review B,* vol. 41, no. 11, pp. 7892-7895, 1990.

[176] G. Kresse and J. Furthmüller, “Efficient iterative schemes for ab initio total-energy calculations using a plane-wave basis set,” *Physical review B,* vol. 54, no. 16, p. 11169, 1996.

[177] J.P. Perdew, K. Burke and M. Ernzerhof, “Generalized gradient approximation made simple,” *Physical review letters,,* vol. 77, no. 18, pp. 11169-11186, 1996.

[178] S. Grimme, J. Antony, S. Ehrlich and H. Krieg, “A consistent and accurate ab initio parametrization of density functional dispersion correction (DFT-D) for the 94 elements H-Pu,” *the Journal of chemical physics,* vol. 132, no. 15, p. 154104, 2010.

[179] S. Grimme, S. Ehrlich and L. Goerigk, ““Effect of the damping function in dispersion corrected density functional theory,” *Journal of computational chemistry,* vol. 32, no. 7, pp. 1456-1465, 2011.

[180] P.E. Blöchl, O. Jepsen and O.K. Andersen, “Improved tetrahedron method for Brillouin-zone integrations,” *Physical Review B,* vol. 49, no. 23, pp. 16223-16233, 1994.

[181] S.L. Dudarev, G.A Botton, S.Y. Savrasov, C.J. Humphreys and A.P. Sutton, “Electron-energy-loss spectra and the structural stability of nickel oxide: An LSDA+ U study,” *Physical Review B,* vol. 57, no. 3, pp. 1505-1509, 1998.

[182] J.M. Seddon and J.D. Gale, Thermodynamics and statistical mechanics, Cambridge: Royal Society of Chemistry, 2001.

[183] Z. Zhou and B. Joos, “Stability criteria for homogeneously stressed materials and the calculation of elastic constants,” *Physical Review B,* vol. 54, no. 6, pp. 3841-3850, 1996.

[184] O. Beckstein, J.E. Klepeis, G.L.W. Hart and O. Pankratov, “First-principles elastic constants and

electronic structure of α- Pt 2 Si and PtSi," *Physical Review B,* vol. 63, no. 13, p. 134112, 2001.

[185] B.B. Karki, G.J. Ackland and J. Crain, "Elastic instabilities in crystals from ab initio stress-strain relations," *Journal of Physics: Condensed Matter,* vol. 9, no. 41, pp. 8579-8589, 1997.

[186] A.J.M Spencer, H.G. Hopkins and M.J. Seweli, "Mechanics of solids," *The R. Hill 60th Anniversary Vol.(Ed. Hopkins and Sewell,* vol. 607, 1982.

[187] M. Tang and S. Yip, "Lattice instability in B-SiC and simulation of brittle fracture," *Journal of Physical Review B,* vol. 52, no. 17, pp. 12627-12635, 1995.

[188] J. Wang, J. Li, S. Yip, S. Phillpot and D. Wolf, "Mechanical instabilities of homogeneous crystals," *Physical Review B,* vol. 52, no. 17, pp. 12627-12635, 1995.

[189] T.H.K. Barron and M.L. Klein, "Second-order elastic constants of a solid under stress," *Proceeding of the Physical Society,* vol. 85, no. 3, p. 523, 1965.

[190] C. Kittel, "Introduction to solid state physics," New York, Wiley, 1976.

[191] M.L. Cohen, "Calculation of bulk moduli of diamond and zinc-blende solids," *Physical Review B,* vol. 45, no. 367, pp. 823-843, 1985.

[192] S. Pugh, "XCII. Relations between the elastic moduli and the plastic properties of polycrystalline pure metals," *The London, Edinburgh, and Dublin Philosophical Magazine and Journal of Science,* vol. 45, no. 367, pp. 823-843, 1954.

[193] S.F. Pugh, "XCII. Relations between the elastic moduli and the plastic properties of polycrystalline pure metals," *The London, Edinburgh, and Dublin Philosophical Magazine and Journal of Science,* vol. 45, no. 367, pp. 823-843, 1954.

[194] D. Alfè, "PHON: A program to calculate phonons using the small displacement method," *Computer Physics Communication,* vol. 180, no. 12, pp. 2622-2633, 2009.

[195] M. Tuccillo, O. Palumbo, M. Palumbo, A. Paolone and S. Brutti, "Analysis of the Phase Stability of $LiMO_2$ Layered Oxides (M = Co, Mn, Ni)," *crystals,* vol. 10, no. 526, p. 2, 2020.

[196] L. Wang, T. Maxisch, and G. Ceder, "Oxidation energies of transition metal oxides within the GGA+ U framework," *Phys. Rev. B,* vol. 73, p. 195107, 2006.

[197] X. Li, Q. Wang, H. Guo, N. Artrith and A. Urban, "Understanding the Onset of Surface Degradation in $LiNiO_2$ Cathodes," *ACS Applied Energy Materials,* vol. 5, p. 5731, 2022.

[198] K. Parlinski, Z.Q. Li, Y. Kawazoe, "First-principles determination of the soft mode in cubic ZrO_2," *Physical Review Letters,* vol. 78, no. 21, p. 4063, 1997.

[199] S. Pugh, "XCII. Relations between the elastic moduli and the plastic properties of polycrystalline pure metals," *The London, Edinburgh, and Dublin Philosophical Magazine and Journal of Science,* vol. 45, no. 367, pp. 823 - 843, 1954.

[200] V.N. Kothalawala, A.A. Devi, J. Nokelainen, M. Alatalo, B. Barbiellin, T. Hu, U. Lassi, K. Suzuki, H. Sakurai and A. Bansil, "First Principles Calculations of the Optical Response of $LiNiO_2$,"

Condesed matter, vol. 7, no. 54, pp. 3-9, 2022.

[201] M.E. Baloyi, P.E. Ngoepe and H.R. Chauke, “Effect of Gadolinium rare-earth element on Nd2Fe14B permanent magnet,” *RAPDASA-RobMech-PRASA-CoSAAMI Conference,* vol. 370, pp. 1-7, 2022.

[202] F.D. Hardcastle and I.E. Wachs, “Determination of niobium-oxygen bond distances and bond orders by Raman spectroscopy,” *Solid State lonics ,* vol. 45 , pp. 201-213, 1991.

[203] Y. Kim, “First principles investigation of the structure and stability of $LiNiO_2$ doped with Co and Mn,” *J. Mater. Sci.,* vol. 47, p. 7558–7563, 2012.

[204] Q. Zhao, J. Wang, Y. Cui, X. Ai, Z. Chen, C. Cao, F. Xu, and Y. Gao, “The discovery of conductive ionic bonds in NiO/Ni transparent counter electrodes for electrochromic smart windows with an ultra-long cycling life,” *Advance materials,* vol. 2, pp. 4667-4676, 2021.

Appendix A:

Papers Presented at Conferences

1. Fits principle study of Lithium Nickel Oxide and Surface stability, CHPC National Meeting, CSIR ICC (November 2022).
2. Structural, mechanical and electronical properties of Lithium Nickel Oxide Bulk ($LiNiO_2$) and surface stability, South African Institute of Physics (67^{th}), University of Zululand, (July 2023).
3. Ab-initio studies of lithium nickel oxide and its surface stability, Faculty of Science and Agriculture Research Day, Bolivia Lodge (13^{th}), (September 2023)
4. Effects of Nb and Mn doping on the pristine $LiNiO_2$ surface: DFT+U study, CHPC National Meeting, Skukuza (December 2023).
5. The effects of Nb/Mn doping on $LiNiO_2$ (101) surface and its interaction with ethylene carbonate electrolyte, South African Institute of Physics (68^{th}), Rhodes University, (July 2024).
6. The effect of surface Nb doping on $LiNiO_2$ (101) surface and its interaction with ethylene carbonate electrolyte: DFT+U study, Faculty of Science and Agriculture Research Day, The Ranch Hotel(14^{th}), (September 2024).
7. The Impact of Mn doping on $LiNiO_2$ (101) surface and its interaction with ethylene carbonate electrolyte: DFT+U study. CHPC National Meeting, Gqeberha. (December 2024).

Papers to be submitted.

1. Computational Modelling Study of Layered $LiNiO_2$, Surface, Surface Doping, and Interaction with the Electrolyte in Li-ion Batteries. MJ Hiine, B Ramogayana, PE Ngoepe and KP Maenetja, to be submitted.